

AD-A100 289

X-RAY TOPOGRAPHIC STUDIES OF ENERGETIC MATERIALS(U)

1/1

STRATHCLYDE UNIV GLASGOW (SCOTLAND)

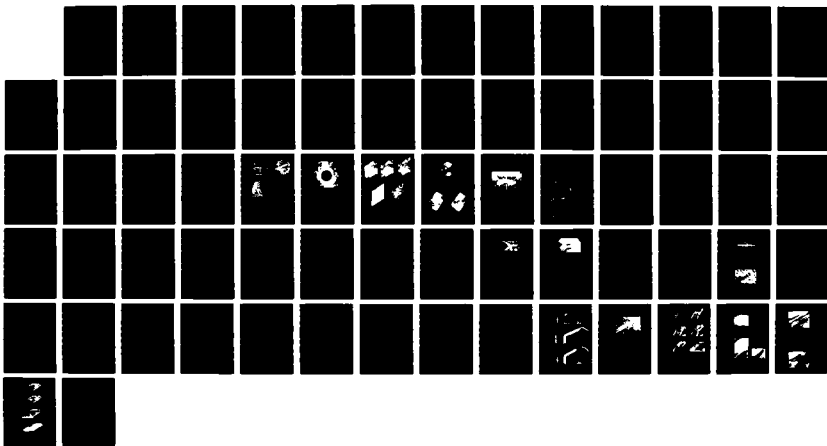
H G GALLAGHER ET AL. MAR 87 R/D-2376A-CH-01

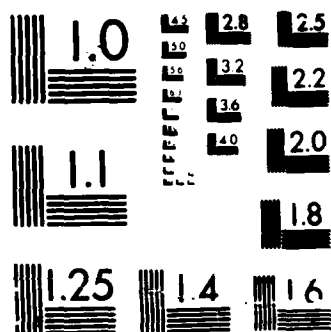
UNCLASSIFIED

DAJA45-83-C-0035

F/G 19/1

ML





MICROCOPY RESOLUTION TEST CHART  
NATIONAL BUREAU OF STANDARDS-1963-A

DTIC FILE COPY

9

AD

AD-A180 289

X-RAY TOPOGRAPHIC STUDIES OF ENERGETIC MATERIALS

by

Hugh G Gallagher  
John C Miller  
John N Sherwood

FINAL REPORT  
March 1987

United States Army  
EUROPEAN RESEARCH OFFICE FOR THE U.S. ARMY  
London, England.

Contract Number DAJA-15-83-6-085

Professor John N. Sherwood  
University of Strathclyde

MAY 13 1987

Approved for Public Release; distribution unlimited.

A180289

REPORT DOCUMENTATION PAGE				Form Approved OMB No 0704 0188 Exp Date Jun 30 1986	
1a REPORT SECURITY CLASSIFICATION UNCLASSIFIED			1b RESTRICTIVE MARKINGS NONE		
2a SECURITY CLASSIFICATION AUTHORITY USAPDSG-UK			3 DISTRIBUTION/AVAILABILITY OF REPORT  APPROVED FOR PUBLIC RELEASE; DISTRIBUTION UNLIMITED		
2b DECLASSIFICATION/DOWNGRADING SCHEDULE NOT APPLICABLE					
4 PERFORMING ORGANIZATION REPORT NUMBER(S)			5 MONITORING ORGANIZATION REPORT NUMBER(S) RD 2376A-CH-01 FINAL REPORT		
6a NAME OF PERFORMING ORGANIZATION UNIVERSITY OF STRATHCLYDE, U.K.		6b OFFICE SYMBOL (If applicable)		7a NAME OF MONITORING ORGANIZATION USAPDSG-UK	
6c ADDRESS (City, State, and ZIP Code) THOMAS GRAHAM BUILDING 295 CATHEDRAL STREET GLASGOW G1 1XL			7b ADDRESS (City, State, and ZIP Code) P.O. BOX 65 FPO NEW YORK, 09510-1500		
8a NAME OF FUNDING/SPONSORING ORGANIZATION EUROPEAN RESEARCH OFFICE		8b OFFICE SYMBOL (If applicable) USAPDSG-UK		9 PROCUREMENT INSTRUMENT IDENTIFICATION NUMBER  CONTRACT # DAJA 45-83-C-0035	
8c ADDRESS (City, State, and ZIP Code)  223 OLD MARYLEBONE RD. LONDON NW1 5TH, U.K.			10 SOURCE OF FUNDING NUMBERS		
			PROGRAM ELEMENT NO 61102A	PROJECT NO 1161102BH57-02	TASK NO 2 WORK UNIT ACCESSION NO
11. TITLE (Include Security Classification)  (U) "X-RAY TOPOGRAPHIC STUDIES OF ENERGETIC MATERIALS"					
12 PERSONAL AUTHOR(S) PROFESSOR J. N. SHERWOOD					
13a TYPE OF REPORT FINAL		13b TIME COVERED FROM 82/12/23 TO 86/9/30		14 DATE OF REPORT (Year, Month, Day) 86/03/01	
15 PAGE COUNT 63					
16 SUPPLEMENTARY NOTATION  NONE					
17 COSATI CODES			18 SUBJECT TERMS (Continue on reverse if necessary and identify by block number)		
FIELD	GROUP	SUB-GROUP	Energetic Materials, Detonation, PETN, RDX, Single Crystals, Crystal Growth, Crystal Perfection, Dislocations, Mechanical Properties, Dislocation Slip, Mechanical Deformation.		
19 ABSTRACT (Continue on reverse if necessary and identify by block number)  <div style="text-align: center;"><u>SUMMARY</u></div> <p>The initial reports on this series of studies (DAERO-78-G-078 and DAJA-37-81-M-0395) were concerned principally with the preparation of high quality crystalline samples of RDX, PETN and TNT for topographic examination. An analysis of the growth defect structure was carried out and the Burgers vectors of the growth defects were defined.</p> <p style="text-align: right;">(see over/..</p>					
20 DISTRIBUTION/AVAILABILITY OF ABSTRACT <input checked="" type="checkbox"/> UNCLASSIFIED UNLIMITED <input checked="" type="checkbox"/> SAME AS RPT <input checked="" type="checkbox"/> DTIC USERS			21 ABSTRACT SECURITY CLASSIFICATION UNCLASSIFIED		
22a NAME OF RESPONSIBLE INDIVIDUAL DR. ROBERT CAMPBELL, CHIEF, CHEMISTRY &			22b TELEPHONE (Include Area Code) 409-4423		22c OFFICE SYMBOL RC

In the present study, these examinations have been extended to the definition of the principal deformation mechanisms in PETN and RDX. This definition has come from detailed experimental and theoretical examinations of the orientation dependence of Knoop microhardness indentations on the habit faces and on cut and polished faces of the crystals, combined with etching experiments. These examinations have been supplemented by "in-situ" deformation studies coupled with X-ray topographic examination of the deformed crystals. The influence of radiation damage from the synchrotron and laboratory sources used for X-ray topographic study have been assessed.

The following principal deformation mechanisms were defined or confirmed

RDX	dislocation slip	(010) [001] and {021} [100]
PETN	dislocation slip	{110} $\langle \bar{1}11 \rangle$

**KEYWORDS** Energetic Materials, Detonation, PETN, RDX, Single Crystals, Crystal Growth, Crystal Perfection, Dislocations, Mechanical Properties, Dislocation Slip, Mechanical Deformation.

## SUMMARY

The initial reports in this series of studies (DAERO-78-G-078 and DAJA-37-81-M-0395) were concerned principally with the preparation of high quality crystalline samples of RDX, PETN and TNT for topographic examination. An analysis of the growth defect structure was carried out and the Burgers vectors of the growth defects were defined.

In the present study, these examinations have been extended to the definition of the principal deformation mechanisms in PETN and RDX. This definition has come from detailed experimental and theoretical examinations of the orientation dependence of Knoop microhardness indentations on the habit faces and on cut and polished faces of the crystals, combined with etching experiments. These examinations have been supplemented by ~~in-situ~~ deformation studies coupled with X-ray topographic examination of the deformed crystals. The influence of radiation damage from the synchrotron and laboratory sources used for X-ray topographic study have been assessed.

The following principal deformation mechanisms were defined or confirmed

RDX	dislocation slip	(010) [001] and {021} [100]
PETN	dislocation slip	{110} $\langle \bar{1}11 \rangle$

KEYWORDS: Energetic Materials, Detonation, PETN, RDX, Single Crystals, Crystal Growth, Crystal Perfection, Dislocations, Mechanical Properties, Dislocation Slip, Mechanical Deformation.



## C O N T E N T S

	Page No.
INTRODUCTION	1
1 Basis and Progress of Programme	3
1.1 Experimental Techniques	3
1.2 Materials	3
1.3 Summary of Progress	4
THE DEFINITION OF DISLOCATION SLIP SYSTEMS IN CYCLOTRIMETHYLENE TRINITRAMINE (RDX)	7
1 Introduction	8
2 Microhardness Measurements	9
2.1 Experimental	9
2.2 Results	9
2.3 Theoretical Analysis and Discussion	10
3 X-ray Topographic Studies	13
3.1 Preliminary Assessment	14
3.2 Radiation Damage Studies	14
3.3 Tensile Testing	16
3.4 Microhardness Impressions	17
4 Summary	19
THE IDENTIFICATION OF THE DISLOCATION SLIP SYSTEM IN PETN USING MICROHARDNESS INDENTATION TECHNIQUES	33
1 Introduction	34
2 Experimental	35
2.1 Crystal Preparation	35
2.2 Microhardness Measurements	35
2.3 Etching Conditions	36
3 Results	36
3.1 Knoop Indentation	36
3.1.1 (110) face	36
3.1.2 (101) face	37
3.2 Calculation of the ERSS	37
3.2.1 Choice of Slip Systems	37
3.2.2 (110) face	38
3.2.3 (101) face	39
3.3 Dislocation Etching of Indentations	39
4 Discussion	40
5 Conclusions	41
AN X-RAY TOPOGRAPHIC STUDY OF MECHANICALLY INDUCED DISLOCATIONS IN PETN	49
1 Introduction	50
2 Experimental	50
2.1 Crystal Preparation	50
2.2 Deformation Methods	51
2.2.1 Microhardness Indentation	51
2.2.2 'In-situ' Tensile Testing	51
2.3 X-ray Topography	51
3 Results	52
3.1 Indentation Deformation	52
3.2 Characterisation of the Dislocation Loops	54
3.3 Tensile Deformation	54
4 Conclusions	56

## Introduction

It is accepted generally that the impact initiation of solid energetic materials occurs by the transfer of mechanical energy into heat within small volumes (hot spots) in the material. Despite this agreement on the potential source of the initiation, there is considerable controversy as to the basic mechanism by which the transfer of energy occurs.

Field [1-3] has summarised the possible macroscopic mechanisms by which this might occur as:

- (i) Adiabatic compression of trapped gas space.
- (ii) Viscous heating of material rapidly extruded between impacting surfaces or grains.
- (iii) Friction between the impacting surfaces, and/or the explosive crystals, and/or grit particles in the explosion layer.
- (iv) Localised adiabatic shear of the materials during failure.

The role of macroscopic mechanical deformation of the explosive is inherent in all of these mechanisms. It has been emphasized by more specific experiments. For example, Kholevo [4] has shown that the sensitiveness of explosives to impact initiation can be reduced if the sample is prevented from flowing. Also, Heavens and Field [1] and Field, Swallowe and Heavens [3] have shown that plastic flow and even melting does occur during impact initiation. The last study also demonstrated that initiation can occur following fragmentation or melting of the solid and not necessarily in the bulk crystalline state.

Encouraged by information of this type, several workers have proposed mechanical mechanisms for the build up of energy. Afanasev and Bobolev [5] suggested a fracture based mechanism in which "hot spots" are formed by the release of energy along slip



surfaces at the onset of gross mechanical failure. At the more microscopic level, Fox and Soria-Ruiz [6,7] have shown that high temperatures can indeed be generated at the tips of moving cracks and have suggested that this could lead to initiation. Field and his co-workers [3] reject this single crack theory on the basis that the energy produced is too low to give the necessary temperature and size of "hot spot". They do note, however, that the energy of fracture can cause chemical decomposition to gaseous products which in turn could be adiabatically compressed to yield ignition. Thus a mechanical basis remains.

An alternative microscopic approach taken by Coffey [8], Coffey and Armstrong [9] and by Elban and Armstrong [10] is to associate dislocation motion with initiation. They propose that the impact causes dislocations to be driven along slip planes. Dissipation of the kinetic energy of the moving dislocations leads to local heating of the crystal and, potentially, the formation of hot spots. This theory again suffers from the problem that the energy gained is low and the volume heated will be small when compared with the anticipated hot spot size. The local concentration of energy generated by the sudden collapse of a dislocation pile-up allows for much greater rises in temperature, although these drawbacks remain.

Despite this potential involvement of mechanical deformation in the initiation process, there has been little attempt to investigate and define the nature and properties of lattice defects in energetic materials, their role in micro-plasticity and the relationship of this to macro-plasticity and hence initiation. The present series of studies was commenced in an effort to redress this situation. Such information is also useful, however, in relation to the changes which might occur in the development of sub-structures in energetic materials during storage and thermal treatment. For example, such changes may yield voids or gas spaces which could influence the sensitivity of the stored material. It is also relevant to the general mechanical behaviour of such solids in preparation and packing.

## 1 Basis and Progress of Programme

The principal aims of the programme were (1) to examine and define the nature and properties of the commonly occurring lattice defects in organic secondary explosive materials and (2) to assess the role of these defects in crystal growth and in the microplasticity of the solid.

### 1.1 Experimental Techniques

The method chosen for the detailed studies of the dislocation structure was X-ray topography [11]. This technique has the advantage that it can be used for the characterisation of the bulk defect structure of large samples ( $1\text{cm}^3$ ) provided that they are of high quality ( $<10^5$  dislocations  $\text{cm}^{-2}$ ). It can also be used under ambient conditions with sensitive or reactive materials which could decompose under more extreme conditions, such as, for example, in the high electron fluxes of the electron microscope.

The examinations can be readily extended to detailed studies of the microplasticity of the materials using stress/strain stages designed to fit the X-ray topographic camera. This allows the behaviour of the defects to be examined "in-situ" under stress and their development assessed.

In addition to the above, and to provide complementary evidence on mechanical behaviour, studies of bulk deformation were carried out by microhardness indentation and dislocation etching techniques.

### 1.2 Materials

The materials chosen for examination in the full programme were

Pentaerythritol tetranitrate (PETN)  
Cyclotrimethylene trinitramine (RDX)

### 1.3 Summary of Progress

For this type of examination, a necessary pre-requisite is the availability of large, high quality, single crystals. A considerable part of the initial contract was devoted to the determination of conditions required for the production of such crystals. Satisfactory procedures were developed for the production of large (5-10cm<sup>3</sup>) highly perfect crystals of PETN and RDX.

Using these samples, detailed studies have been made of the principal deformation mechanisms in this type of organic material.

Deformation of the samples was achieved by one or both of two methods; microhardness testing using a Leitz microhardness indentation tester with a Knoop indenter and tensile testing using a micro-tensile apparatus.

Both materials were examined using the former method. The Knoop indenter allows the orientation dependence of microhardness to be assessed and produces a variation in hardness which is related to the geometry of the emergent slip or twinning system at the crystal surface. In all cases, the experimental curve was compared with a theoretical assessment of the hardness variation derived for several potential deformation systems. Trial and error curve fitting in this way allowed the definition of the most likely potential slip systems for the materials concerned. Such comparisons have been made successfully for the simple crystallographic systems. This is the first time that the models have been applied to the more complicated, highly anisotropic structures and dislocation slip systems characteristic of organic molecular solids.

In most cases, the potential slips systems were confirmed from the distribution and orientation of dislocation etch patterns produced by the etching of microhardness indentations. This method of attack was supplemented by X-ray topographic studies of the strain distribution around the microhardness impressions.

Using the information derived from these examinations, more detailed studies were made. The availability of basic information on the orientation and character of the slip systems allowed the possibility of oriented gross deformation to produce dislocation slip. Tensile deformation was attempted to produce slip in particular slip systems.

In RDX, at room temperature, slip could not be initiated. Samples deformed elastically to fracture. More success was achieved with PETN confirming its greater plasticity relative to RDX. Tensile tests initiated slip on the  $\{110\}$  planes. Edge indentation generated dislocation loops in the same planes. These experiments confirmed the more speculative results of the microhardness measurements. Deformation to fracture resulted in massive dislocation multiplication.

X-ray topographic studies were carried out to define the Burgers vectors  $\underline{b}$  of the dislocation types. These studies defined  $\underline{b} \langle 111 \rangle$ , an orientation in good agreement with the etch-pit shape and alignment. Thus we define the principal slip system of PETN unambiguously as  $\{110\} \langle \bar{1}11 \rangle$ .

## REFERENCES

1. S.N. Heavens and J.E. Field, Proc. Roy. Soc., A338, 77 (1974).
2. G.M. Swallowe and J.E. Field, Proc. Roy. Soc., A379, 389 (1982).
3. J.E. Field, G.M. Swallowe and S.N. Heavens, Proc. Roy. Soc., A382, 231 (1982).
4. N.A. Kholevo, Trudy Kazan. Khim. Tech. Inso., 10, 91 (1946).
5. G.T. Afanasev and V.K. Bobolev, Initiation of Solid Explosives by Impact, Israel Program for Scientific Translations, Jerusalem 1971.
6. P.G. Fox and J.Soria Ruiz, Proc. Roy. Soc., A317, 79 (1970).
7. P.G. Fox, J. Solid State Chem., 2, 491 (1970).
8. C.S. Coffey, Phys. Revs., B24 (1981).
9. C.S. Coffey and R.W. Armstrong, Shock Waves and High Strain Rate Phenomena in Metals: Concepts and Applications, Editors M.A. Mayer and L.E. Muir (Plenum, New York) 1981, p. 313.
10. W.L. Elban and R.W. Armstrong, 7th International Symposium on Detonation, Annapolis, Maryland (US Office of Naval Research) 1981.
11. B.K. Tanner and D.K Bowen, Editors 'Studies of Growth Defects in Crystals using X-Ray Methods', NATO-ASI No. B63, Durham, UK, 1979, Plenum, NY 1980.

THE DEFINITION OF DISLOCATION SLIP SYSTEMS  
IN CYCLOTRIMETHYLENE TRINITRAMINE (RDX)

- 1 Introduction
- 2 Microhardness Measurements
  - 2.1 Experimental
  - 2.2 Results
  - 2.3 Theoretical Analysis  
and Discussion
- 3 X-ray Topographic Studies
  - 3.1 Preliminary Assessment
  - 3.2 Radiation Damage  
Studies
  - 3.3 Tensile Tests
  - 3.4 Micro-hardness Impressions
- 4 Summary

APPENDIX

## 1 Introduction

Examination of the orientation and alignment of dislocation etch-pit traces on the habit surfaces of RDX single crystals have led to the proposition that three potential slip systems are active in this material. Following an examination of the  $\{210\}$  growth surfaces of strained and unstrained crystals Connick and May [1] proposed (010) as the dominant slip plane. In a subsequent similar examination, Elban and Armstrong [2] found no evidence for alignments of this orientation and, on the basis of their observations, argued strongly for  $\{021\}$  as the major slip plane. Since this would involve dislocations of Burgers vector greater than those potentially available on (010) they rationalised their choice by proposing that motion occurred via dissociation of the most likely unit vector into partials.

Some resolution of this difference of opinion came from the later Vickers microindentation hardness examination of Halfpenny, Roberts and Sherwood [3]. By etching microhardness impressions on the  $\{210\}$ ,  $\{111\}$  and (001) habit surfaces these authors confirmed that dislocation slip was the dominant deformation mechanism. The primary slip plane was identified as (010). These authors also identified a secondary slip plane as  $\{021\}$  or  $\{011\}$  but, due to the small area covered by the slip patterns, they were unable to distinguish between these alternatives.

In order to make a better definition of the slip systems in these materials, we have extended these studies to a Knoop microindentation hardness study of the anisotropy of surface hardness. The results have been correlated with a theoretical analysis of the orientation dependence of the effective resolved shear stress (ERSS) acting on the bulk of the crystal computed on the basis of the proposed slip systems [4,5]. Such analyses have been applied successfully to ionic solids and metals of a variety of crystallographic structures, but usually of a high crystallographic symmetry. The present application to an anisotropic molecular solid shows both the application of the approach to this type of solid and also indicates the breadth of utility of the analysis.

## 2 Microhardness Measurements

### 2.1 Experimental

Indentation microhardness measurements were carried out using a Leitz Miniload indentation hardness system fitted with a standard Knoop indenter. Indentations (15g load at ambient temperature, 291K) were made on a {210} habit face of RDX. The crystals were grown by the slow evaporation of saturated acetone solutions. The conditions of growth and general perfection of the product have been described previously [6]. Indentations were made at 5° intervals as the crystal was rotated around the normal to a {210} face. Zero was fixed with the long diagonal of the indenter parallel to the intersection of (010) with the surface. The length of the long diagonal was used to calculate the Knoop hardness number (KHN).

Slip traces produced by indentation were etched in acetone at ambient temperature followed by a rapid quench in water [3]. This process revealed distinct etch-pits along the slip-lines.

### 2.2 Results

Well defined and regular impressions resulted at all angles other than at  $90^\circ \pm 5^\circ$ . Within this range, cracks formed along the intersection of the (001) plane with the surface. These were more obvious following etching than on direct examination.

The experimentally determined variation in KHN with orientation is shown in Figure 1.

Each experimental point represents an average of the results from ten indentations. The KHN varies considerably with orientation ( $32\text{--}44 \text{ Kg mm}^{-2}$ ) proving the considerable anisotropy of hardness of RDX. This variation peaks at  $40^\circ$  and  $140^\circ$  displaced from the (010) intersection and forms a trough at  $90^\circ$  and  $0^\circ/180^\circ$  displacement. The depth of the trough at  $90^\circ$  is



presumably overemphasised by the cracking which accompanies indentation at this orientation. This anisotropy should reflect the crystal structure of the solid and the orientation of its active dislocation slip systems relative to the surface.

### 2.3 Theoretical Analysis and Discussion

A theoretical analysis of the effective resolved shear stress was carried out using both the classic analysis of Daniels and Dunn [4] and the modified equation of Brookes et al [5]. The Daniels and Dunn equation expresses the ERSS ( $\tau_e$ ) in the form

$$\tau_e = F/A \cos \lambda \cos \phi \cos \psi$$

where  $F$  is the applied force,  $A$  the cross sectional area of the specimen,  $\lambda$  is the angle between the stress axis and the slip direction,  $\phi$  the angle between the stress axis and the normal to the slip plane and  $\psi$  is the angle between a horizontal axis lying parallel to the indenter face and the axis of rotation of the slip system (see Figure 2).

The Brookes equation states

$$\tau_e = F/A \cos \lambda \cos \phi \frac{1}{2} (\cos \psi + \cos \gamma)$$

where, in addition to the other terms defined above,  $\gamma$  is the angle between a horizontal axis lying parallel to the indenter face and the slip direction.

In the development of the above equations, it was assumed that the crystal being deformed was made up from a large number of very small cylinders all aligned parallel to the deforming force,  $F$ , with  $F$  being parallel to the steepest slope of the indenter facet. The factor  $\tau = F/A \cos \lambda \cos \phi$  thus follows from the well-established Schmid and Boas relationship for the plastic deformation of crystals. Under stress, it is well-defined that each cylinder will undergo lattice rotation and

tend to elongate. Daniels and Dunn argued that in a single crystal, lattice rotation is likely to be hindered by neighbouring cylinders. To account for this, they introduced a constraint factor ( $\Psi$ ) with the constraint being maximum at  $\Psi = 90^\circ$  and minimum at  $\Psi = 0^\circ$  (see Figure 2). A consequence of this is that when  $\Psi = 90^\circ$ ,  $\cos \Psi = 0$  and hence  $\tau_e = 0$ . Under these geometrical conditions, however, Brookes et al found etch-pit alignments following indentation of MgO showing that there is an ERSS acting on the crystal at this orientation. To account for this, Brookes et al included the further constraint factor  $\gamma$  noted above. Their new constraint term is  $\frac{1}{2}(\cos \Psi + \sin \gamma)$ . Now the maximum constraint will occur at  $\gamma=0^\circ$ ,  $\Psi=90^\circ$ . Indentation of MgO at an orientation giving  $\gamma=0^\circ$ ,  $\Psi=90^\circ$  for two of their indenter facets gave no etch-pit alignments at these facets. At the other two facets for which  $\gamma \neq 0^\circ$ ,  $\Psi=90^\circ$  a small ERSS is predicted and etch-pit alignments were produced. Brookes has since applied this analysis successfully to a number of crystalline solids. It must be added, however, that the Daniels and Dunn analysis has been equally successful in predicting the behaviour of other materials.

The present theoretical curves were calculated using a stereographic projection of the indenter, a stereographic projection of RDX and a Wulff net. The stereographic projection of the indenter, showing also the position of the principal slip system, is shown schematically in Figure 3. The calculations were made for the (010), (021) and (02 $\bar{1}$ ) potential slip planes assuming that the Burgers vector of the mobile dislocations corresponded to the shortest lattice translation in each case, viz (010) [001], (021) [100] and (02 $\bar{1}$ ) [100]. No assessment was made of the possible influence of the potential {011} slip systems on hardness, since no evidence was found for this in the present study. The term  $F/A$  in the expressions for ERSS cannot be determined absolutely in a hardness test. It should, however, be constant at constant load and the trigonometric factors can be used to define the variation in relative ERSS with orientation.

The theoretical ERSS is averaged over all four facets with the slip system that has the greatest ERSS being assumed to be in operation at that orientation. KHN is inversely proportional to ERSS, i.e. the higher the ERSS, the greater the slip and hence the softer the material. The theoretical ERSS curve should therefore mirror the experimental KHN curve.

Figures 4 and 5 show the results of using both the Daniels and Dunn and Brookes analyses for the  $(021)$ ,  $(02\bar{1})$  and  $(010)$  slip systems. The solid line on each figure represents a combination of the calculated ERSS for both slip systems with the system of highest ERSS at a particular orientation being deemed to operate. We cannot account presently for the dip at  $90^\circ$  orientation in the Brookes analysis. Despite this, both analyses show excellent general agreement with the experimental hardness results. Both predict that the  $\{021\}$  slip systems dominate when the long diagonal of the indenter lies parallel to  $[001]$ . As the ERSS for  $\{021\}$  decreases with orientation, so that for  $(010)$  increases until at  $35^\circ$ - $58^\circ$  clockwise from  $[001]$  a change-over point occurs where both slip systems should have an equivalent ERSS. From  $60^\circ$ ,  $(010)$  becomes increasingly dominant reaching a maximum at  $90^\circ$  and then decreasing to  $130^\circ$ - $150^\circ$  when another change-over point is reached. Finally  $\{021\}$  dominates from  $150^\circ$  to  $180^\circ$ .

The orientation dependence of the ERSS as predicted by the theoretical curve was confirmed by solvent etching of the hardness indentations. Figure 6a shows an etched indentation made with the long axis parallel to  $[001]$ . Distinct dislocation etch-pit alignments can be seen parallel to the lines of intersection of the  $(021)$  and  $(02\bar{1})$  planes with the surface. This supports the predicted dominance of these slip systems at this orientation. When an indentation is made at  $155^\circ$  from  $[001]$  etching reveals both  $\{021\}$  and  $(010)$  alignments (Figure 6b), although the occurrence of slip, simultaneously, on both systems spoils the resolution to some extent. Severe cracking of the surface occurs when indentations are made at  $90^\circ$  to  $[001]$  and alignments of etch-pits along the intersection of  $(010)$  with the surface are best seen at an orientation of  $65^\circ$  (Figure 6c) where, according to the calculations, slip on  $(010)$  should still be dominant.

This combination of the excellent agreement between the shape and phase of the experimental and calculated curves together with the activation of the expected slip traces at the predicted indenter orientation provides strong evidence for (010), (021) and (02 $\bar{1}$ ) slip planes. From this we may speculate that the dislocations involved in the process are of the types (010) [001], (021) [100] and (02 $\bar{1}$ ) [100]. These correspond to high energy dislocation types and are consistent with the low plasticity of the crystal and the limited range of dispersion of dislocation etch-pits around the indentation marks.

These results show well the applicability of this type of analysis to anisotropic organic molecular crystals.

### 3 X-ray Topographic Studies

Following the definition of the potential slip systems in RDX by comparison of the theoretical and experimental studies of microhardness, an attempt was made to initiate slip and to characterise the resulting dislocations using X-ray topography [7].

The principal limitation to the use of monochromatic X-ray topography in the characterisation of mechanical deformation processes 'in-situ' is the lack of availability of suitable X-ray reflections for the characterisation process. This problem is often exacerbated by the orientation of the sample which is defined by the deformation experiments and is not necessarily the most suitable orientation for topographic study. The situation is made worse with organic materials which present few X-ray reflections of suitably high structure factor to yield good topographic images. These constraints can often be overcome by the use of synchrotron radiation sources where the high intensity, broad spectrum X-radiation can permit the recording of satisfactory images of low structure factor reflections. Also, under some conditions of exposure, a multiplicity of images can be obtained simultaneously and on short exposure. Potentially

the use of synchrotron sources can permit the rapid evaluation and characterisation of dislocation slip processes in all materials. A prime limitation of the technique, however, is that the high intensity source can cause radiation damage to samples. This can be severe with reactive materials such as those presently under examination.

### 3.1 Preliminary Assessment

An initial assessment was made of the potential use of the 'Laue' synchrotron topography technique for the recording of multiple images from a suitably cut RDX crystal. The crystal section was placed with its largest, (001), face normal to the synchrotron beam and a large area photographic plate placed behind it to record a full crystal Laue pattern. The result (2 mins exposure, 1 GeV, 200ma) is shown in Figure 7.

As can be seen, a multiplicity of images are obtained, many of these are indistinct and of too low quality to allow their use for dislocation analysis. There are also a satisfactory number of well-contrasted reflections. Continued exposure resulted, however, in a deterioration of the images in a manner consistent with the onset of radiation damage in the sample.

### 3.2 Radiation Damage Studies

Due to the indistinct images from the above specimen an assessment of the course and rate of synchrotron radiation damage was made using a specimen of slice plane (001) suitably oriented to yield the well-contrasted  $4\bar{2}0$  reflection (Figure 8 ).

Exposure of the crystal to the full synchrotron beam (2 GeV, 200ma,  $\lambda=0.1\text{\AA} \sim 4\text{\AA}$ ) for a few minutes led to the rapid yellow discolouration of the previously colourless transparent sample. Over a total period of 10 minutes, the topographic image rapidly deteriorated due to the development of increasing strain in the sample until finally no structure could be discerned. Despite

this rapid deterioration in structural quality, the sample remained transparent. Over a further period of days following exposure the yellow colouration faded to yield a milky white discolouration.

We interpret this train of events as follows. The yellow colouration arises from the formation of colour centres in the crystal. This is accompanied by chemical decomposition to yield gaseous products. Over the post-irradiation period these aggregate to give the milky-white discolouration which possibly represents colloid centres in the crystal.

Synchrotron radiation damage of this kind is predominantly a consequence of the ready absorption of the longer wavelength components of the spectrum. Under such circumstances, it should be possible to prolong the life of the specimen by the attenuation of the softer components from the incident beam. Insertion of a 1mm aluminium absorber between the incoming beam and the specimen effectively absorbs all radiation of wavelengths  $\geq 1\text{\AA}$ . Under these conditions, severe deterioration of the specimens can be delayed for up to 1 hour (Figure 8).

The structural changes which accompany decomposition develop from strained regions of the crystal around the interface between the seed and the newly grown crystal and at strained volumes in the growth sectors. These are distinguishable generally as areas of darker contrast in the topograph (see Figure 8). As radiolysis continues, the increase in strain and decomposition leads to an acceleration of the reaction. Similar influences of lattice strain on reactivity have been noted by us for other solid state reactions such as thermal and radiolytic dehydration reactions and solid-state polymerisation [8].

It is noteworthy that the dislocation structure of the sample is not affected by the radiolytic process. For example, in Figure 8, isolated dislocations (A) and bundles of dislocations (B) show little change in contrast or position during

irradiation. Thus they are not the nuclei of the reaction, neither do they move under the induced stress of the decomposition process. The latter observation is consistent with the general low plasticity of this solid.

In contrast to their behaviour under synchrotron radiation, the lifetime of RDX crystals during topographic analysis on a laboratory-based sealed-beam tube under normal operating conditions (40kV , 20 ma) was "infinite". No changes in substructure were observed even after a multiplicity of exposures. In-situ tensile experiments were carried out under these laboratory conditions and using the synchrotron source with the beam attenuated with a 1mm aluminium absorber.

### 3.3 Tensile Tests

The choice of a suitable sample orientation which might allow the development of a satisfactory resolved shear stress for both the  $\{021\}$   $[100]$  and  $(010)$   $[001]$  slip systems plus access to satisfactory topographic reflections proved impossible. Table 1 shows the potential orientations and available X-ray reflections.

TABLE 1

Specimen Plane	Tensile Axis	Slip activated	Useful X-ray Reflections
(010)	(101) <sub>n</sub>	$\{021\}$ $[100]$	002
(001)	(110) <sub>n</sub> or (210) <sub>n</sub>	$\{021\}$ $[100]$	420 220
(100)	(011) <sub>n</sub>	(010) $[001]$	021, 023, 022
{111}	[121]	$\{021\}$ $[100]$	-
		(010) $[001]$	-

$(hkl)_n$  denotes the normal to the plane  $(hkl)$ .

Initial experiments were carried out with a sample of slice plane (001) and tensile axis  $(110)_n$ .

The sample was cut from the central region of the crystal section shown in Figure 9. The sample contained two large dislocation bundles and a number of single growth dislocations with irregular line directions similar to those characterised as  $b[010]$  by Halfpenny et al [9]. The sample  $1 \times 0.5 \times 0.1 \text{ cm}^3$  was chemically polished, fixed between the jaws of a microtensile straining stage [10] and the whole mounted on the topographic camera. X-ray topographs were taken using synchrotron radiation of  $\lambda = 0.7\text{\AA}$  ( $\mu\text{t} \approx 1.5$ ).

The sample was put under tension. The strain was increased in increments and a topograph recorded following each incremental change until fracture occurred. Figure 10 shows topographs of the crystal before straining and immediately prior to fracture. The only noticeable difference between the two images is the increased background strain which could arise from radiation damage rather than mechanical deformation. No mechanical dislocations have been induced neither have existing non-linear dislocations moved.

This lack of dislocation slip under the conditions used is consistent with the low plasticity of this solid as exemplified by the microhardness measurements. Further experiments are in process of development to test the other sample orientations and to assess the influence of temperature on the slip process.

### 3.4 Microhardness Impressions

Further evidence for the nature of the slip systems in RDX was sought from the contrast distribution of X-ray topographic images of Vickers microhardness indentations. Due to the lack of accessibility of satisfactory X-ray reflections for indentations made on the major  $\{210\}$  habit faces, assessments were restricted to indentations made on cut and polished  $(001)$  faces. Vickers indentation was used to provide a more isotropic deformation than Knoop indentation.



Figure 11 shows an etched Vickers microhardness impression (50g load) on a (001) habit surface [3]. From the well-defined pyramidal impression, a central, highly deformed region spreads  $100\mu\text{m}$  along the [010] direction. This is surrounded by etch-pits decorating a larger volume ( $200\mu\text{m}$ ) and which again align along [100]. This alignment is consistent with the fact that all three potential slip systems; (021),  $(02\bar{1})$  and (010) intersect this face in this orientation. Thus, potentially, the etch-pits represent the emergent ends of dislocations gliding on all three slip planes and induced by the indentation.

X-ray transmission topographs of similar Vickers impressions (25g and 50g load) are shown in Figure 12. The images comprise a central linear  $150\mu\text{m}$  wide "out of contrast" portion lying parallel to [100], surrounded by a black lobed contrast figure the long axis of which lies parallel to the "g" direction. The centre "out of contrast" portion can be seen best at image A in the 200 reflection. In other reflections, it is hidden or distorted by the surrounding black lobed contrast. The size, orientation and negative contrast of this central portion is consistent with it corresponding to the central highly deformed region noticable in Figure 11. On this basis, any of the dislocation images which may have formed around the periphery of this region will be masked by the extent of the lobed darker contrast. Hence, they cannot be identified or characterised.

The black lobed contrast figure corresponds to elastic strain which is developed into the surrounding lattice during the indentation process. It extends (impression B) to  $700\mu\text{m}$  from the site of the impression and falls off to zero over a further  $300\mu\text{m}$  (the fringe pattern). The similarity of the size of the images in all three reflections suggests that, despite the high anisotropy of the plastic deformation process, the elastic strain develops more uniformly around the impression. This type of behaviour, wide-spread development of elastic strain, is characteristic of a highly brittle material. It confirms that considerable elastic strain would have to be developed in the

solid before plastic deformation will occur. On this basis, it is not surprising that it proved impossible to generate slip in the tensile experiment before fracture occurred. Further experiments are in course to test the temperature dependence of the elastic/plastic deformation process.

#### 4 Summary

Knoop hardness measurements on the  $\{210\}$  surfaces of RDX crystals show an orientation dependence consistent with a high anisotropy of mechanical deformation. Theoretical analyses of these variations based on potential dislocation slip systems derived from previous studies show that this orientation dependence could be explained on the basis of slip on two potential systems  $(010) [001]$  and  $\{021\} [100]$ . This possibility was confirmed in part by etching studies of Knoop indentation marks.

An attempt to provide absolute confirmation of this proposal by tensile tests coupled with X-ray topography was defeated by the low plasticity of the material at room temperature. Under these conditions the material proved to be elastic to fracture.

#### REFERENCES

- 1 W. Connick and F. G. J. May, J. Crystal Growth, 5 (1969) 165.
- 2 W. Elban and R. W. Armstrong, Seventh Int. Symposium on Detonation, Annapolis, Maryland, 1981.
- 3 P. J. Halfpenny, K. J. Roberts and J. N. Sherwood, J. Materials Sci., 19 (1984) 1629.
- 4 F. W. Daniels and C. G. Dunn, Trans. ASM, 41, 419 (1949).
- 5 C. A. Brookes, J. B. O'Neill and B. A. W. Redfern, Proc. Roy. Soc. London, A322, 73 (1971).
- 6 P. J. Halfpenny, K. J. Roberts and J. N. Sherwood, J. Crystal Growth, 69, (1984), 73.
- 7 B. K. Tanner and D. K. Bowen, Editors; "Studies of Growth Defects in Crystals Using X-ray Methods", NATO-ASI, No. B63, Plenum, N.Y., 1980.

- 8 D. B. Sheen and J. N. Sherwood, Chem. Brit., (1986), 536.
- 9 P. J. Halfpenny, K. J. Roberts and J. N. Sherwood, Phil. Mag., A53, (1986), 531.
- 10 D. K. Bowen and J. Miltat, J. Phys. E., 9, (1976), 868.

### APPENDIX

Since the completion of this work, Armstrong and Elban [1] have proposed that the Burgers vectors of dislocations which glide on the (010) slip plane in RDX should be  $\underline{b}$  [100] and not  $\underline{b}$  [001] as proposed above. Their argument is based on molecular packing diagrams which indicate the possibility that there would be less interference between molecules gliding in the (010) plane in this direction than in the alternative [001] direction.

To test this proposal, we have extended our theoretical calculations to include an assessment of the ERSS variation with orientation assuming that (010) [100] slip will dominate. The result is shown in Figure 13.

The Figure predicts a maximum ERSS at angles of  $0^\circ$  and  $180^\circ$  to [001] and a minimum at  $90^\circ$  to [001]. The combination of this with the predicted variation of ERSS for {021} [100] would not yield the observed maximum ERSS (minimum hardness) at  $90^\circ$  to [001] required by the experimental variation.

We conclude that it is unlikely that the slip system (010) [100] will be dominant in RDX.

- 1 R. W. Armstrong and W. L. Elban, Chem. Prop. Info. Agency, "Microstructural Origin of Hot Spots in RDX Crystals", to be published.

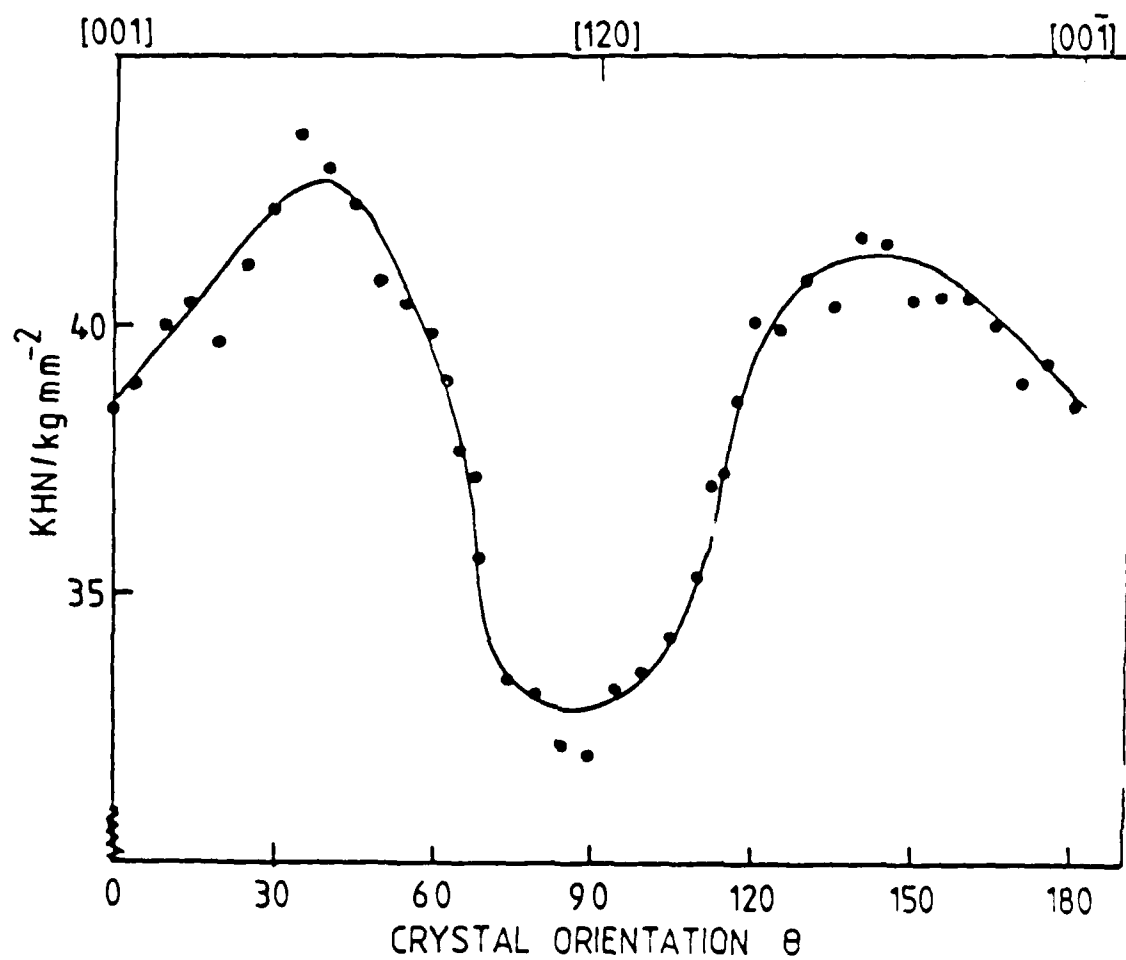
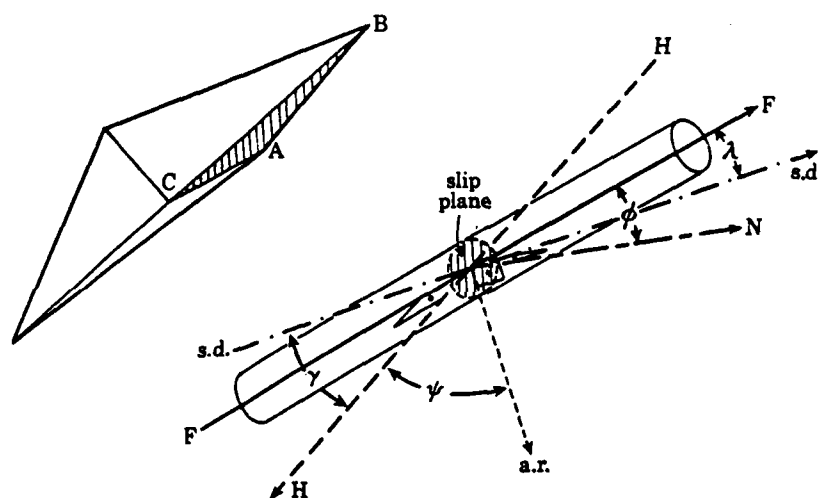


Figure 1 Knoop hardness number (KHN) against crystal orientation ( $\theta$ ) for the (210) habit face of RDX.



A schematic illustration to show the angles  $\phi$ ,  $\lambda$ ,  $\psi$  and  $\gamma$ .  
 FF, Tensile axis; HH, axis parallel to indenter facet ABC; N, slip plane normal;  
 s.d., slip direction; a.r., axis of rotation in slip plane. Note that the angles between  
 FF and HH, s.d. and N and s.d. and a.r. are all constant and equal to  $90^\circ$ . The angles  
 $\phi$ ,  $\lambda$ ,  $\psi$  and  $\gamma$  are determined by indenter: specimen orientation and here ABC is the  
 relevant facet.

Figure 2: after reference [7].

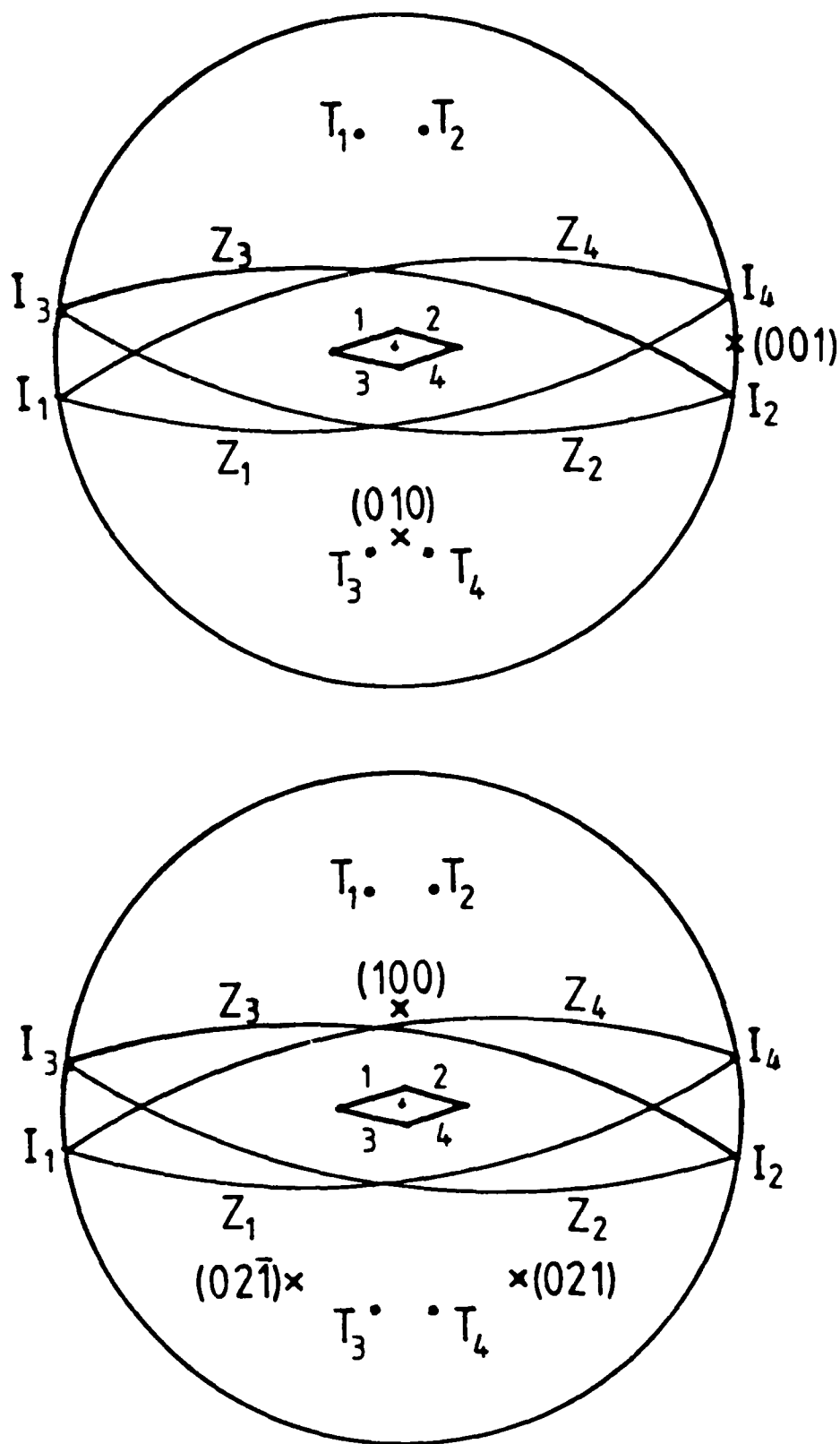


Figure 3: Schematic representation of the stereographic projection of the Knoop indenter with respect to the relevant slip systems.  $T_1$  is the Tensile axis for facet (1),  $I_1$  the horizontal axis parallel to indenter facet (1) and  $Z_1$  is trace of points at  $90^\circ$  to  $T_1$ . Similarly for 2, 3 and 4.

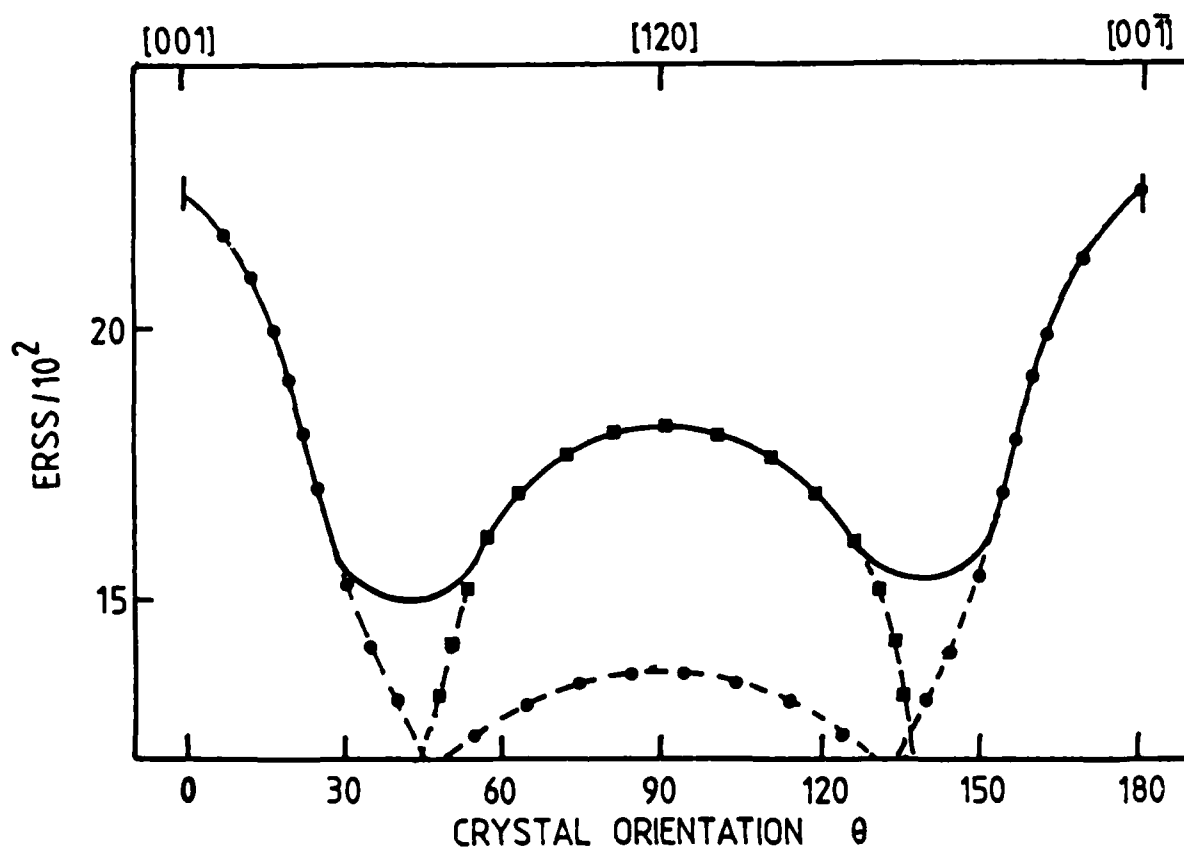


Figure 4

Effective resolved shear stress (ERSS) against crystal orientation after Daniels and Dunn [4] for the slip systems  $\{021\}$  [100] (—●—●—) and (010) [001] (—■—■—).

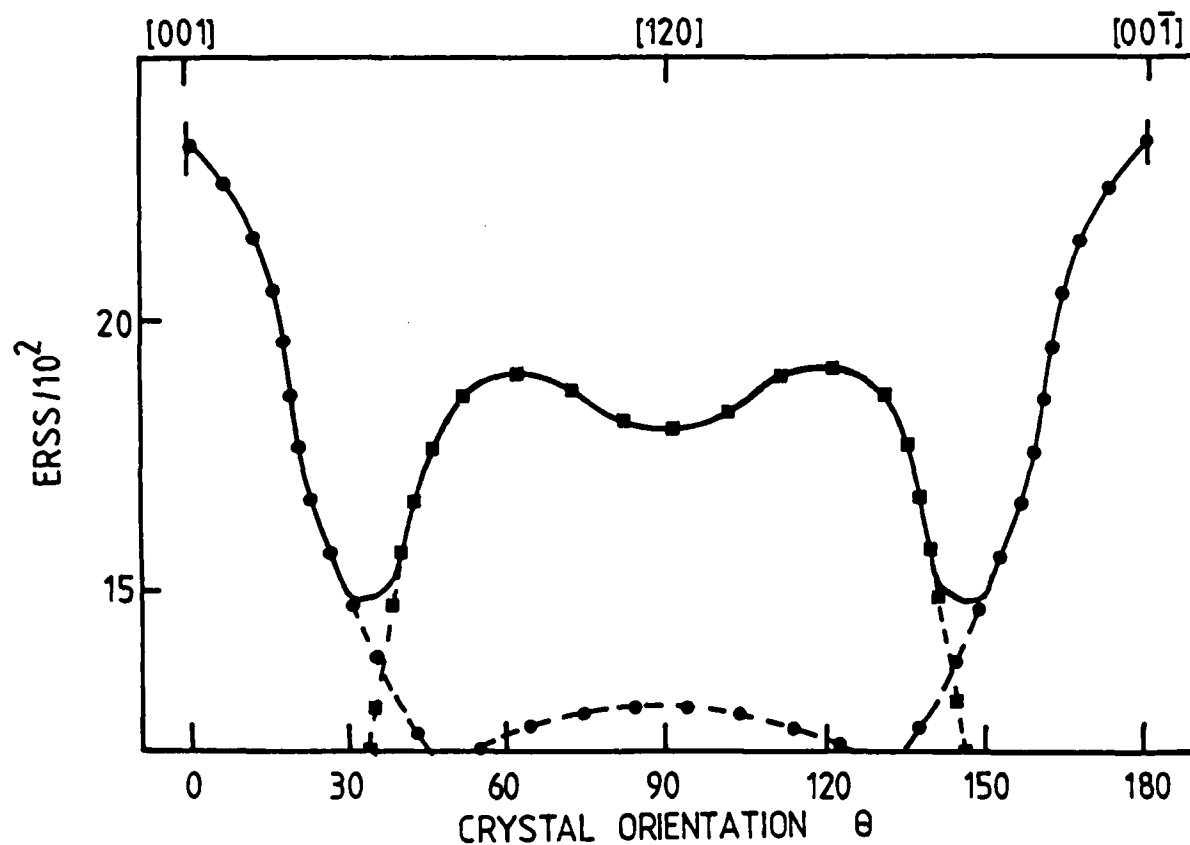
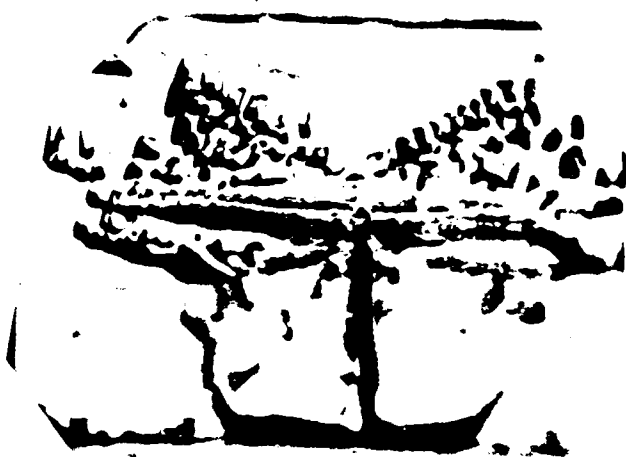


Figure 5

Effective resolved shear stress (ERSS) against crystal orientation after Brookes et al [5] for the slip systems  $\{021\} [100]$  (—●—●—) and  $\{010\} [001]$  (—■—■—).

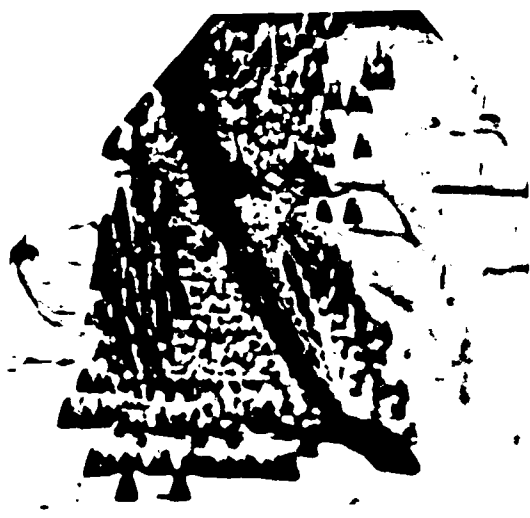




(a)



(b)



(c)

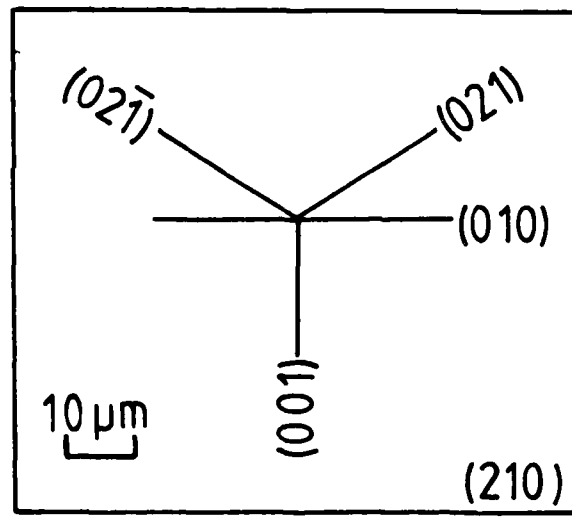
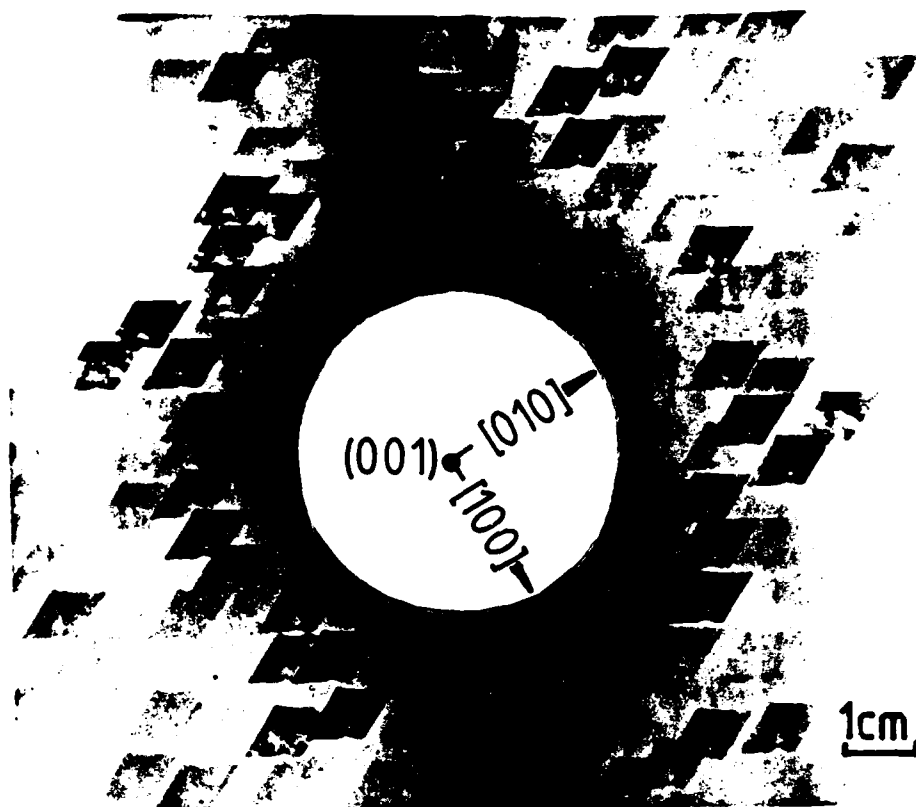
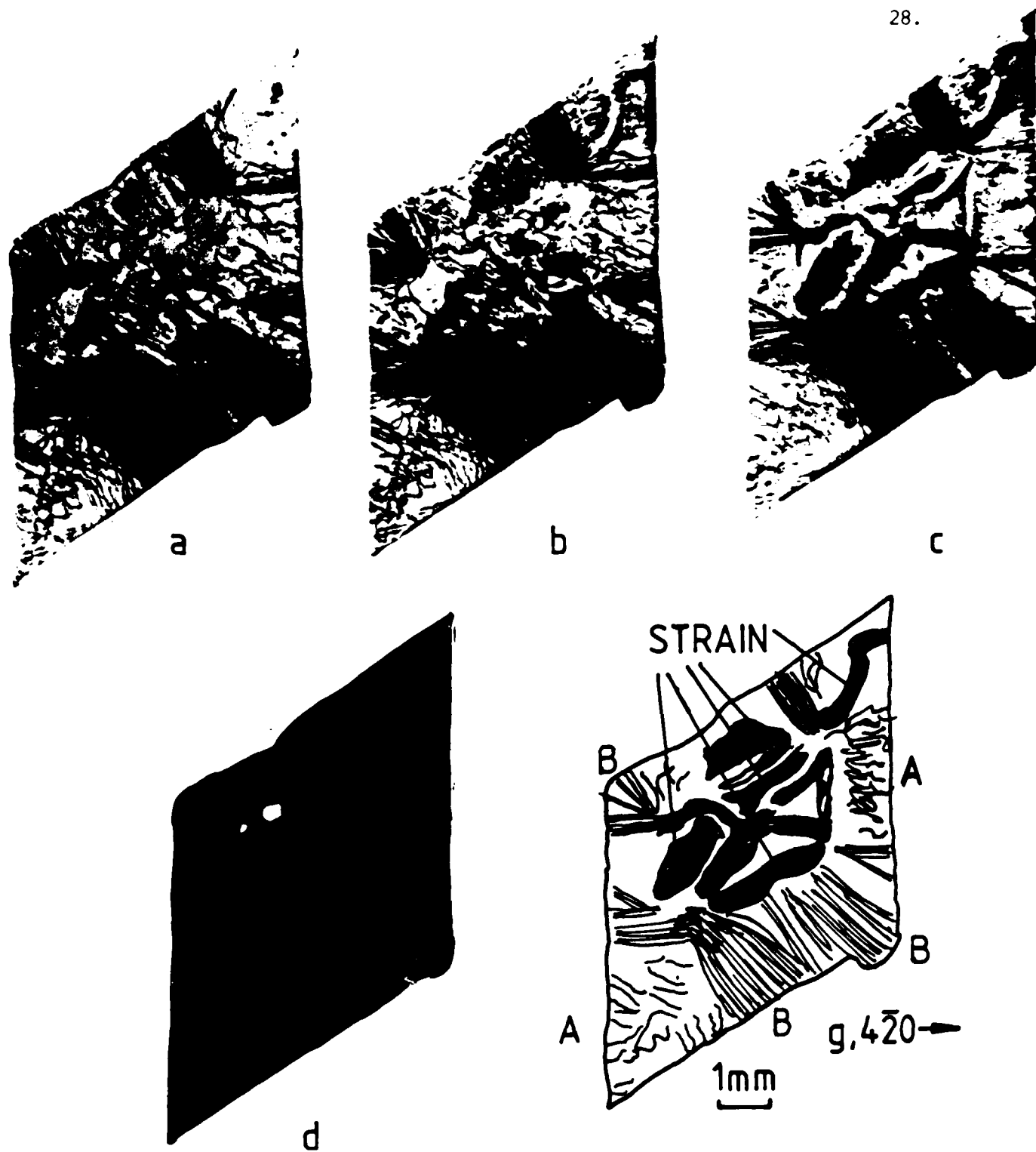


Figure 6: Etch pattern rosettes formed round Knoop indentation marks on a  $\{210\}$  habit surface of RDX. The separate photo micrographs refer to indentations made with the long axis of the indenter (a) parallel (b) at  $155^\circ$  (c) at  $65^\circ$  to  $[001]$ . The inset shows the angles of intersection of the three basic slip planes  $(010)$ ,  $(021)$  and  $(02\bar{1})$  with the surface.



**Figure 7**

Synchrotron Laue topograph of an RDX crystal (001) section ( $\lambda=0.1 \sim 4\text{\AA}$ ). The topograph shows multiple images of different crystal reflections each of which images the defect structure of the crystal. For the most part, the images are diffuse due to the initiation of radiation damage.



**Figure 8**

Synchrotron X-ray topographs ( $4\bar{2}0$  reflection,  $\lambda = 0.7\text{\AA}$ ) of an RDX crystal showing progressive radiation damage on continued exposure (2Gev, 200ma,  $\lambda = 0.1 - 1.0\text{\AA}$ ) (a) initial crystal (b) after 1 hour exposure (c) after 2 hours exposure (d) repeat of (c) 2 days after exposure showing the extent of post-radiation damage which accompanies the formation of colloid centres.

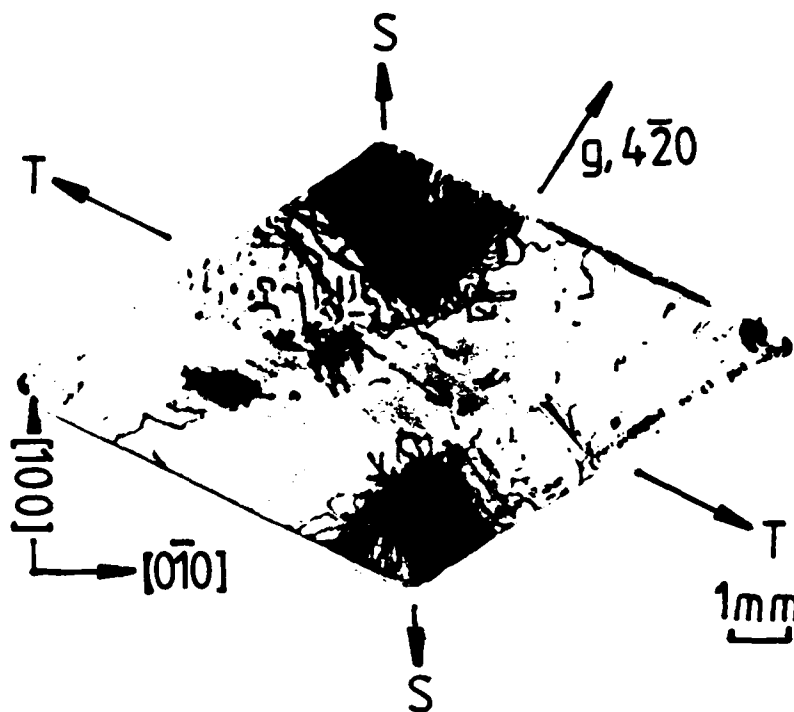


**Figure 9** Topograph ( $4\bar{2}0$  reflection) of a (001) section of an RDX crystal used for the preparation of samples for tensile experiments. T represents the direction of the tensile axis relative to the crystallographic axis and S the intersection of the active slip planes with the crystal plane.

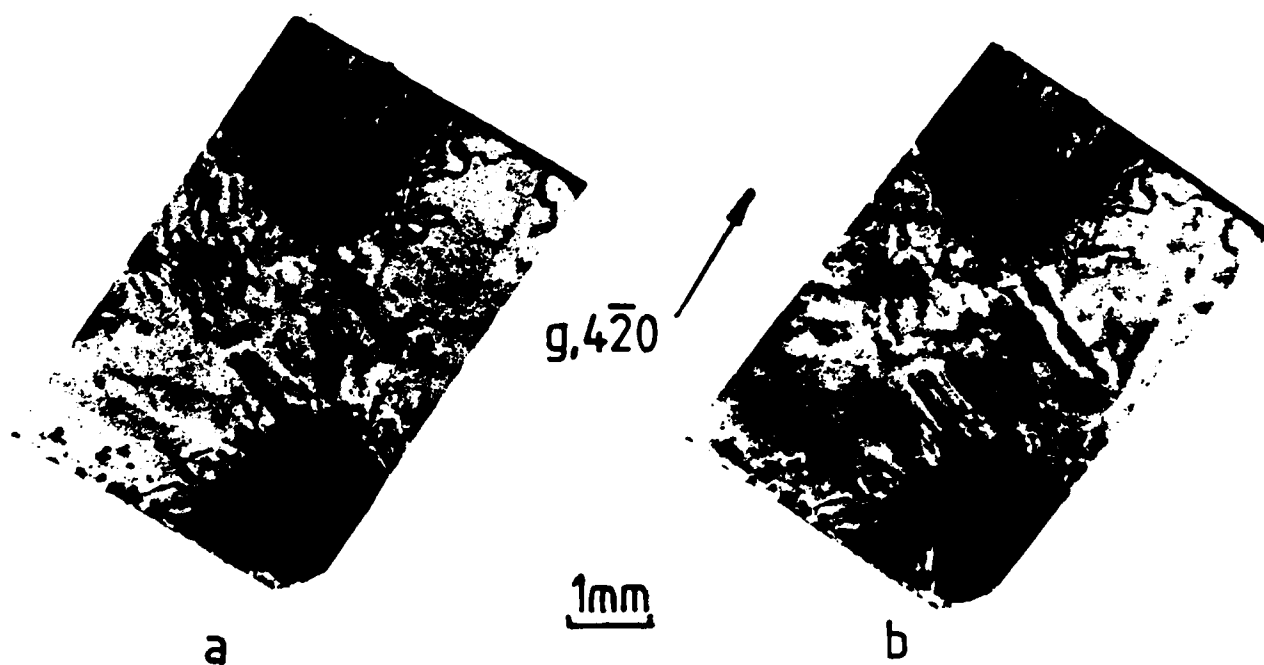


**Figure 10** Topographs ( $4\bar{2}0$  reflections) of the tensile specimen (a) initial (b) immediately prior to fracture.

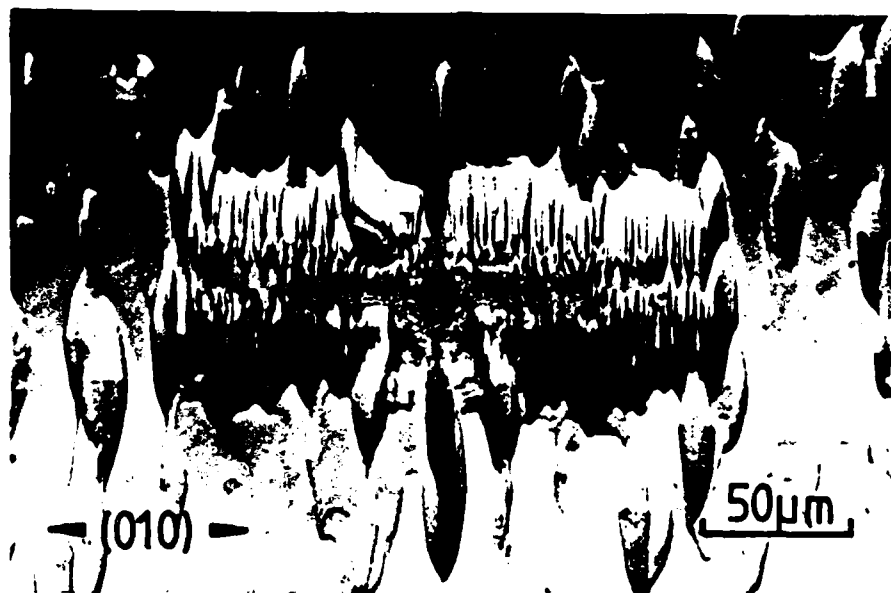


Figure 11 Etched microhardness impression (50g load) on the (001) habit face of RDX.

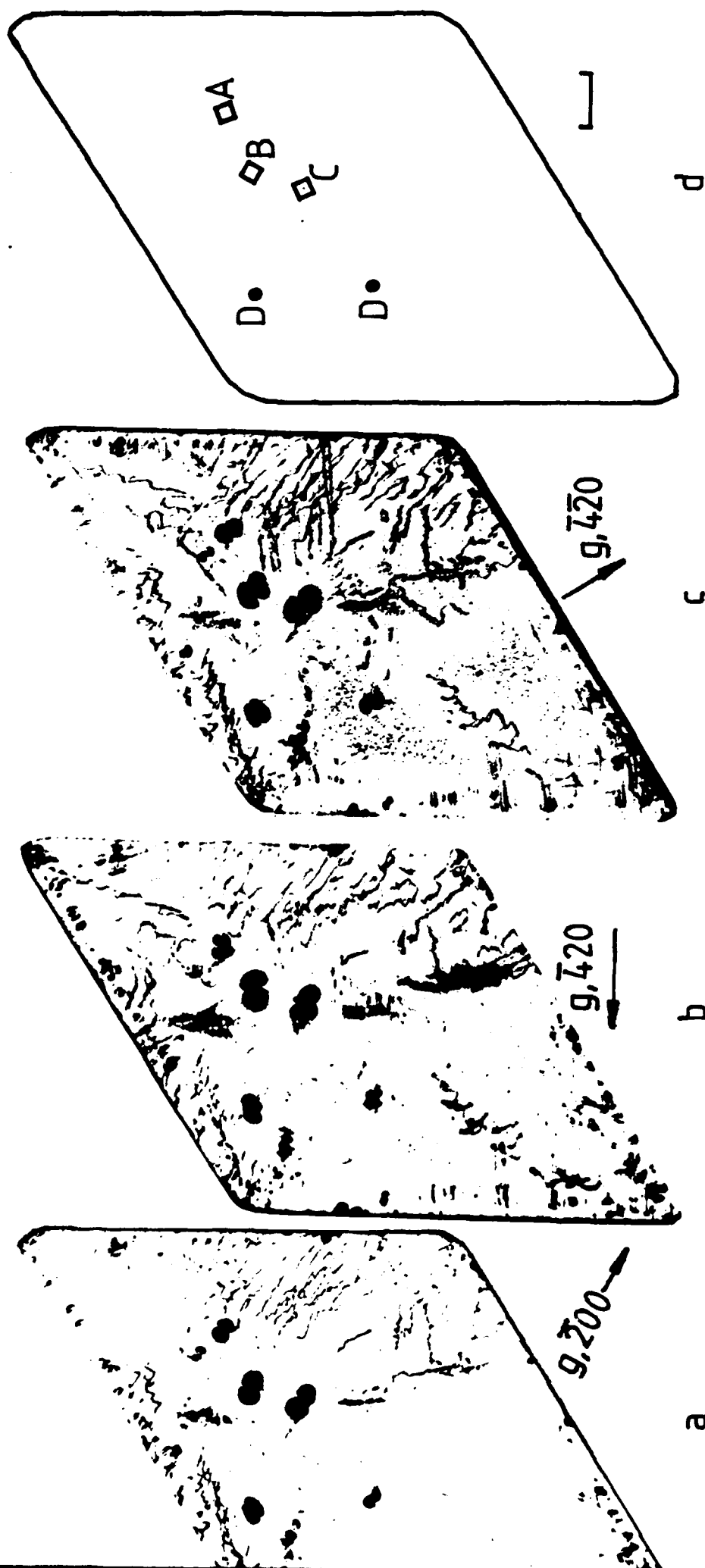


Figure 12 X-ray transmission topographs of Vickers microhardness impressions on a (001) cut and polished face of RDX a) 200 reflection b) 420 reflection c) 420 reflection d) diagram showing the position and orientation of the impressions A 25g, B and C 50g. D are random surface indentations. (Scale mark 1mm).

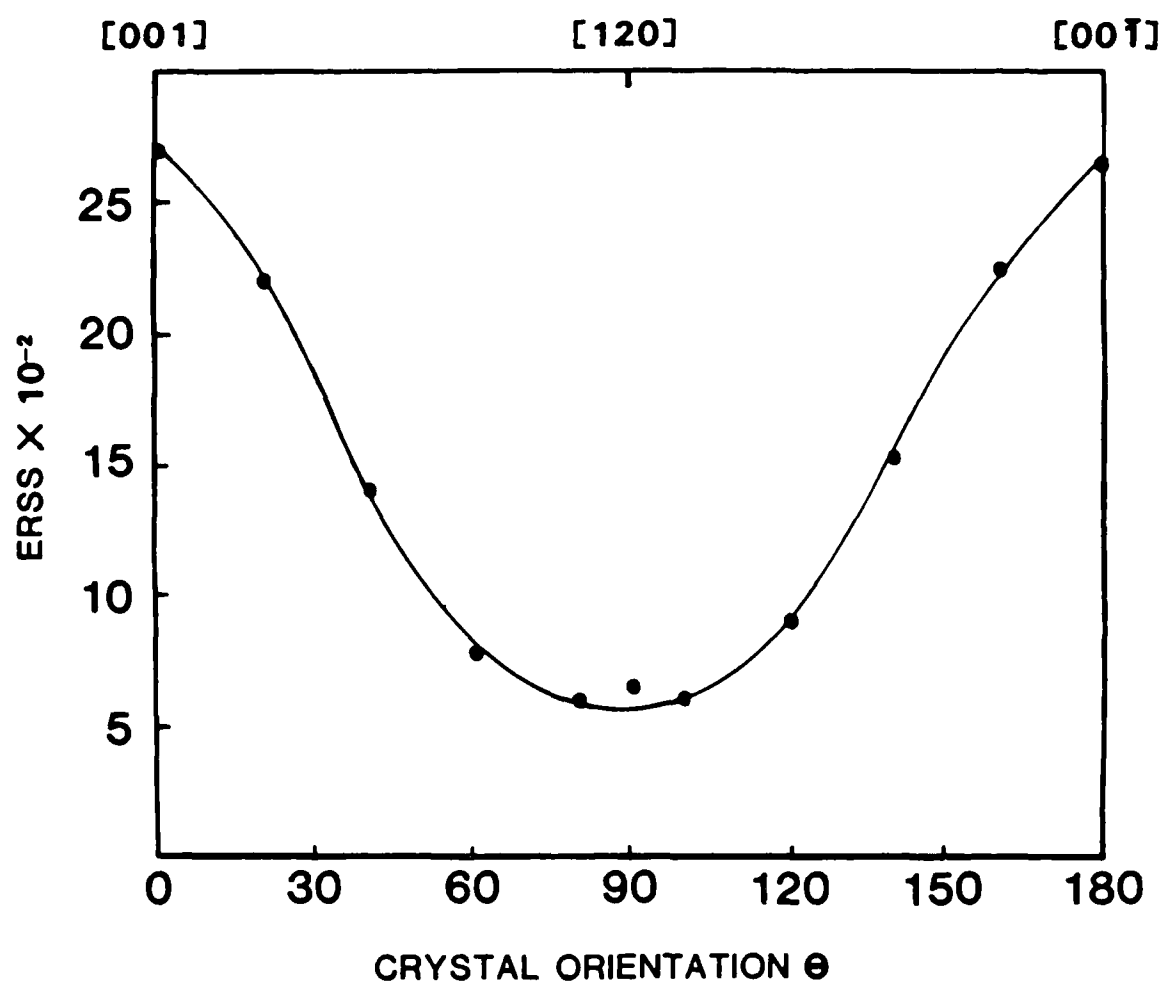


Figure 13 Effective resolved shear stress (ERSS) against crystal orientation after Daniels and Dunn [4] for the slip system (010) [100] in RDX.

THE IDENTIFICATION OF THE DISLOCATION SLIP SYSTEM IN PETN  
USING MICROHARDNESS INDENTATION TECHNIQUES

- 1 Introduction
- 2 Experimental
  - 2.1 Crystal preparation
  - 2.2 Microhardness measurement
  - 2.3 Etching
- 3 Results
  - 3.1 Knoop indentation
    - 3.1.1. (110) face
    - 3.1.2. (101) face
  - 3.2 Calculation of ERSS
    - 3.2.1. Choice of slip systems
    - 3.2.2. (110) face
    - 3.2.3. (101) face
  - 3.3 Dislocation etching of indentations
- 4 Discussion
- 5 Conclusions



## 1 Introduction

There have been two previous microindentation hardness studies of PETN crystals. The first study, by Hagan and Chaudhri [1] was mainly concerned with the fracture properties of the solid, although some evidence for slip was noted. In a later study, Halfpenny et al [2] attempted to define the nature of the dislocations involved in glide. Using a combination of indentation and etching techniques, they showed conclusively that slip occurs on  $\{110\}$  planes. They could only speculate, however, on the nature of the Burgers vectors for dislocation glide on this plane. From consideration of the energy associated with a dislocation, they postulated the lowest unit lattice repeat distance  $[001]$ , as the most likely slip direction.

In the work presented here, an experimental and theoretical comparison of the Knoop hardness anisotropy on both the  $(110)$  and  $(101)$  habit faces was attempted in order to identify the slip systems for PETN.

The variation in Knoop hardness of a wide range of crystalline solids has been successfully explained using the effective resolved shear stress (ERSS) model of Daniels and Dunn [3] and the subsequent modification by Brookes et al [4]. In each of these models, the anisotropy of Knoop hardness is related to the slip systems which govern plastic deformation, taking into account both the Burgers vectors and slip planes of the dislocation systems. The operative slip system is determined by comparing the angular variation of the measured hardness in the surface with the hardness predicted for all potential slip systems. The results from this analysis were supplemented by etching studies.

## 2 Experimental

### 2.1 Crystal preparation

The crystals of PETN were grown from ethyl acetate by both slow cooling of seeded saturated solutions and by solvent evaporation from spontaneously nucleated solutions, following the conditions defined previously by Halfpenny et al [5]. Before use, the PETN (purity 99.75%) was multiply recrystallised from distilled acetone. The crystals exhibited a prismatic habit of well developed {110} and {101} forms, with the former dominant. Typically, the crystals had dimensions  $24 \times 12 \times 10\text{mm}^3$  and weighed between 10g and 15g. The perfection of these crystals was assessed using X-ray diffraction topography. Figure 1 shows an X-ray topograph of a section of a crystal typical of those employed in this study. The crystal is of high overall internal perfection with large volumes entirely free from defects. From this and from other topographs, the dislocation density is estimated to lie in the range  $10 - 10^3$  dislocations per  $\text{cm}^2$ .

### 2.2 Microhardness measurements

The microhardness measurements were made with a Leitz Miniload microhardness tester fitted with a Knoop pyramidal indenter. The Knoop hardness was measured on both the (110) and (101) habit faces as a function of orientation. An indenter load of 15g was used. The load was applied gradually starting from zero, rising to a maximum over a period of 20 secs. The full load was maintained for a further 12 secs before removal. At least 10 indentations were made at each orientation. The reported hardness is the average calculated from these. The hardness measurements were carried out at  $10^\circ$  intervals of rotation from the zero position. On the (110) face, the zero orientation was chosen with the long diagonal of the indenter aligned parallel to [001]. On (101) the zero orientation was fixed as [010].

## 2.3 Etching conditions

The nature of the dislocations associated with the indentations on the (110) face were assessed by etching. Knoop indentations were made using a 25g load and the crystals etched in "Analar" grade acetone for 1 sec at 265K and quenched in water at the same temperature. These etching conditions differ slightly from those reported by Halfpenny et al [2], but were found necessary to ensure adequate resolution of individual pits around the Knoop indentation marks.

## 3 Results

### 3.1 Knoop indentation

#### 3.1.1. (110) face

The variation in hardness with orientation on the (110) face is shown in Figure 2. The Knoop hardness number (KHN) varies in the range 13.0 - 24.4 kg mm<sup>-2</sup>, reflecting a considerable degree of anisotropy. The hard direction is parallel to  $[\bar{1}10]$  and the soft directions lie at  $\pm 15^\circ$  from [001]. The hardness curve shows mirror symmetry about the  $[\bar{1}10]$  direction. This symmetry is consistent with the projection on (110) of the two-dimensional point group symmetry of PETN [6].

Optical examination of the hardness impressions invariably revealed extensive slip traces aligned along [001], as shown in Figure 3. These are characteristic of localised plastic deformation and correspond to the surface intersection of the (110) slip planes. The extent of the slip lines associated with the indentations is a function of orientation, with the maximum and minimum slip occurring when the long axis of the indenter lies long the soft and hard directions respectively.

Some cracking parallel to  $[001]$  is also observed around the indentation marks. The cracks occur as a result of partial cleavage on  $(1\bar{1}0)$  and have been discussed in detail elsewhere [1]. However, it should be noted that the degree of cracking obtained with the Knoop indenter is considerably reduced in comparison with that produced by the Vickers indenter.

### 3.1.2. $(101)$ face

The hardness anisotropy on the  $(101)$  face is presented in Figure 4. The variation in KHN is less pronounced on this face compared with  $(110)$  and ranges between  $14.6 \text{ kg mm}^{-2}$  and  $18.0 \text{ kg mm}^{-2}$ . The position of minimum hardness occurs at  $90^\circ$  from  $[010]$  and the maximum values are obtained at  $\pm 20^\circ$  from this direction. The mirror symmetry displayed by the hardness curve is in agreement with the crystallographic symmetry expected for this face.

Again, extensive slip line traces and some microcracks orientated parallel to the surface intersections of the  $\{110\}$  planes were observed around the indents.

## 3.2 Calculation of the ERSS

### 3.2.1. Choice of slip systems

From the geometry and alignments of the slip traces and dislocation etch pits on both the  $(110)$  and  $(101)$  faces, Halfpenny et al [2] unambiguously defined the slip planes as  $\{110\}$

For a dislocation to move by glide, its Burgers vector must lie in the slip plane. Therefore, the potential Burgers vectors for dislocation glide on  $\{110\}$  are limited to  $[001]$ ,  $\langle 1\bar{1}0 \rangle$  and  $\langle \bar{1}11 \rangle$  ( $|b| = 0.67\text{nm}$ ,  $1.32\text{nm}$  and  $1.48\text{nm}$  respectively). Since the energy of a dislocation is proportional to  $|b|^2$ , Burgers vectors larger than these are highly improbable. As  $[001]$  is the smallest lattice translation, Halfpenny et al [2] proposed this as the most likely slip direction. However, all three possible slip systems were considered in the calculation of ERSS.

### 3.2.2. (110) face

The variation in ERSS with orientation for indentation on the (110) face was calculated for the  $\{110\}$  [001],  $\{110\}$   $\langle\bar{1}10\rangle$  and  $\{110\}$   $\langle\bar{1}11\rangle$  slip systems. The shape of the ERSS curves obtained using the models of Daniels & Dunn [3] and Brookes et al [4] were found to be almost identical, differing only in the magnitude of the ERSS. The curves of ERSS versus orientation for all three systems, based on the latter expression, are shown in Figure 5. (The theoretical background to these models is presented in the section on RDX above.) These curves should mirror the variation of hardness with maximum ERSS corresponding to minimum hardness and vice-versa.

The ERSS curve for  $\{110\}$  [001] slip has a maximum along the  $[\bar{1}10]$  direction and minimum parallel to [001]. This is in direct contradiction to the experimental hardness curve which also has its maximum and minimum along these approximate directions. Therefore,  $\{110\}$  [001] can be discounted as a possible slip system. In contrast, the agreement between the measured hardness and the calculated ERSS for the  $\{110\}$   $\langle\bar{1}10\rangle$  and  $\{110\}$   $\langle\bar{1}11\rangle$  slip systems is much better. In both curves, the position of minimum ERSS is parallel to the  $[\bar{1}10]$  direction, corresponding to the hard direction of surface hardness. However, neither plot gives an exact fit to the experimental data in the region around  $\langle 001 \rangle$ . In each case, the maxima in the theoretical curves are  $15^\circ$  out of phase with the soft directions indicated by the hardness curve.

The discrepancies between the experimentally determined hardness anisotropy and the theoretical curves in the region of [001] may be due to minor differences in crack behaviour at these orientations or, more fundamentally, may result from the basic simplifications inherent in the model. However, it is felt that in both cases the general agreement is acceptable within the limitations of the analysis. Therefore, these results indicate that the operative slip system must be either  $\{110\}$   $\langle\bar{1}10\rangle$  or  $\{110\}$   $\langle\bar{1}11\rangle$ , but does not allow distinction between them.

### 3.2.3. (101) face

In an attempt to distinguish between  $\{110\} \langle \bar{1}10 \rangle$  and  $\{110\} \langle \bar{1}11 \rangle$  slip, an analysis for these two slip systems was undertaken for indentation on the (101) face.

The ERSS curves for  $\{110\} \langle \bar{1}10 \rangle$  and  $\{110\} \langle \bar{1}11 \rangle$  slip are shown in Figure 6. In both curves, the ERSS is maximum along  $[\bar{1}01]$ , corresponding to the soft direction of hardness. The curve for  $\{110\} \langle \bar{1}10 \rangle$  slip also has two minima at the orientations  $\pm 20^\circ$  from  $[010]$ , in good correspondence with the maximum values of Knoop hardness. The curve for the  $\{110\} \langle \bar{1}11 \rangle$  slip system is rather more complex in this region. It exhibits two relatively small peaks which are not apparent in the hardness curve. However, it is highly unlikely that the measured hardness, which has a standard deviation of  $\sim 15\%$ , would be sensitive to such minor variations in ERSS. Bearing this in mind, the two curves are almost equivalent. Therefore, as with the (110) face, the analysis on (101) does not allow distinction to be made between the  $\{110\} \langle \bar{1}10 \rangle$  and  $\{110\} \langle \bar{1}11 \rangle$  slip systems.

### 3.3 Dislocation etching of indentations

Etching of indented (110) faces revealed rows of etch pits extending along well-defined slip line traces around the indentation marks. An optical micrograph of an etched indentation is shown in Figure 7. The etch pits are aligned exclusively along the  $[001]$  direction, corresponding to the intersection of the  $(1\bar{1}0)$  slip planes with the surface. The etch pit morphology and alignments were similar at all orientations of indentation, indicating that only one slip system is active in this solid. Closer examination of the etch pit geometry, as shown in Figure 8, revealed the pits to be hexagonal with mirror symmetry about  $(1\bar{1}0)$ . The apex of the pits is considerably displaced from their geometric centre in the  $[001]$  direction.

Gilman and Johnson [7] have demonstrated that the etch pits formed by local point deformation represent the emergent ends of dislocation loops, probably with the pure edge or screw segments intersecting the surface. The asymmetry of the etch pits suggests that they are associated with dislocations which lie at an oblique angle to the (110) face. Only dislocations with a Burgers vector  $\langle 111 \rangle$  could possibly yield pure edge or screw dislocations for such an inclined dislocation line direction. Analogously, the etch pits formed at the points of emergence of pure dislocations with Burgers vectors [001] or  $\langle 110 \rangle$  would be expected to have their apex coincident with the geometric centre of the pit. No etch pits of this type were observed.

It is likely, therefore, that the etch pits produced around the indentation marks originate at the emergent ends of stress induced dislocation loops which glide on  $(1\bar{1}0)$  planes with Burgers vector  $\langle 111 \rangle$ .

On the (101) face, the etch pits formed at the sites of indentation show similar asymmetry. However, in this case, all three potential Burgers vectors are inclined to the surface. Therefore, it is not possible to speculate about the nature of the dislocations intersecting this face.

#### 4 Discussion

Although some minor fracture corresponding to partial cleavage on  $\{110\}$  planes does occur, the observation of extensive slip steps and dislocation etch pit arrays around the indentations clearly indicates that dislocation glide is the predominant mode of deformation in PETN. The observed variation in the extent of the slip traces and etch pit alignments with indenter orientation reflects the considerable plastic anisotropy of this solid.

Despite its failure to distinguish between the  $\{110\} \langle \bar{1}10 \rangle$  and  $\{110\} \langle \bar{1}11 \rangle$  slip systems, the theoretical analysis does rule out the possibility that  $\{110\} [001]$  is an operative slip system. The inability to distinguish between the two alternatives illustrates a major limitation of the analysis. If the different combinations of slip plane and slip direction contrive to produce a closely similar curve of ERSS, then the slip system cannot be defined conclusively. Often, this can be overcome by carrying out the analysis on a different face. However, in the case of PETN, indentation on both naturally occurring faces did not differentiate between the  $\{110\} \langle \bar{1}10 \rangle$  and  $\{110\} \langle \bar{1}11 \rangle$  slip systems. The asymmetric nature of the pits associated with etched indentations strongly suggests that the latter is the active slip system for PETN.

It is interesting to note that the  $\langle \bar{1}11 \rangle$  Burgers vector is not the shortest lattice translation contained in the slip plane and, therefore, dislocations of this type are high energy dislocations. Pure dislocations of this Burgers vector have been noted previously to be the predominant type of growth dislocation [8] observed by X-ray topography. Whether or not this observation is significant is open to question since growth dislocations are unlikely to be generated by slip processes.

## 5 Conclusions

A theoretical analysis of the experimentally determined Knoop hardness anisotropy has been used to assess the active slip system for PETN. The results obtained from this analysis were supplemented by etching studies. Several conclusions can be derived as follows:

- 1 The Knoop hardness showed considerably anisotropy on both the (110) and (101) habit faces. The KHN varied between 13.0 and 24.4 kg mm<sup>-2</sup> on the (110) face and 14.6 and 18.0 kg mm<sup>-2</sup> on the (101) face. The positions of maximum and minimum hardness did not always correspond to the low index crystallographic directions.



- 2 Comparison of the observed hardness and the hardness predicted by accepted models indicated that the operative slip system could be either  $\{110\} \langle \bar{1}10 \rangle$  and  $\{110\} \langle \bar{1}11 \rangle$ . It was not possible to distinguish between these alternatives. The analysis did, however, rule out  $\{110\} [001]$  as a possible slip system.
- 3 Examination of the slip steps and etch features associated with the indentations confirmed that  $\{110\} [001]$  was not the slip system. The asymmetric geometry of the pits produced around etched indentations on the  $(110)$  face strongly suggested that the dislocations involved in glide have Burgers vector  $\langle 111 \rangle$ . On this basis,  $\{110\} \langle \bar{1}11 \rangle$  is postulated as the dominant slip system for PETN.

### References

- 1 J. T. Hagan and M. M. Chaudhri, J. Mater. Sci., 12, (1977), 1055.
- 2 P. J. Halfpenny, K. J. Roberts and J. N. Sherwood, J. Mater. Sci., 19, (1984) 1629-1637.
- 3 F. W. Daniels and C. G. Dunn, Trans. Am. Soc. Metals, 41, (1949) 419.
- 4 C. A. Brookes, J. B. O'Neill and B. A. W. Redfern, Proc. Roy. Soc. London A, 322, (1971), 73-88.
- 5 P. J. Halfpenny, K. J. Roberts and J. N. Sherwood, J. Cryst. Growth, 67, (1984), 202-212.
- 6 International Tables for X-ray Crystallography, Vol I, (1969), P40, Birmingham : Kynoch Press.
- 7 J. J. Gilman and W. G. Johnston in "Dislocations and Mechanical Properties of Crystals", Ed. J. C. Fisher, Wiley (1957), P116.
- 8 P. J. Halfpenny, K. J. Roberts and J. N. Sherwood, J. Appl. Cryst., 17, (1984), 320-327.

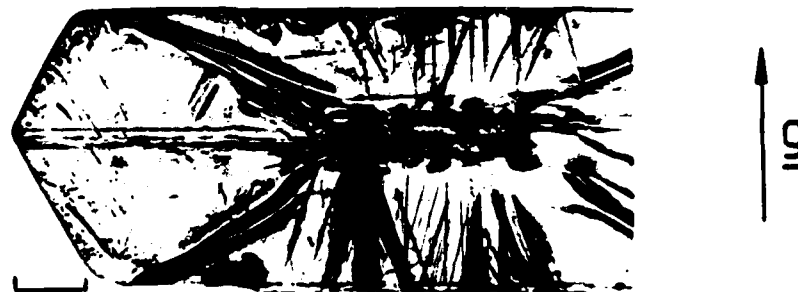


Figure 1 An X-ray topograph of a (110) slice of a PETN crystal showing the high internal perfection. ( $g = 2\bar{2}0$ ,  $\text{Cu } K_{\alpha_1}$  radiation). (Scale mark 1mm)

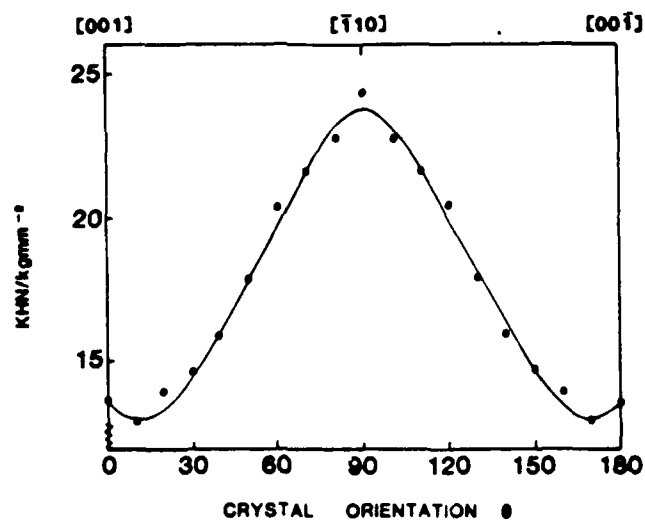


Figure 2 The variation in Knoop hardness number (KHN) with crystal orientation ( $\theta$ ) on the (110) habit face of PETN.



Figure 3 A Knoop hardness impression (load 25g) on the  $(110)$  face of PETN showing extensive slip line traces. (Scale mark  $50\mu\text{m}$ )

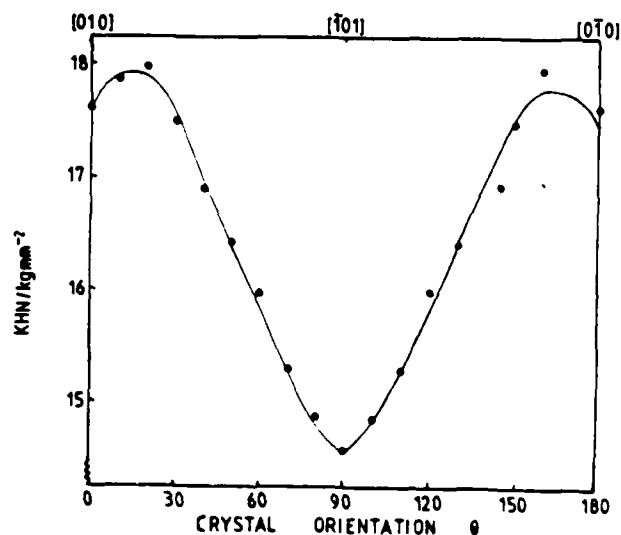


Figure 4 The variation in Knoop hardness number (KHN) with crystal orientation ( $\theta$ ) on the  $(101)$  habit face of PETN.

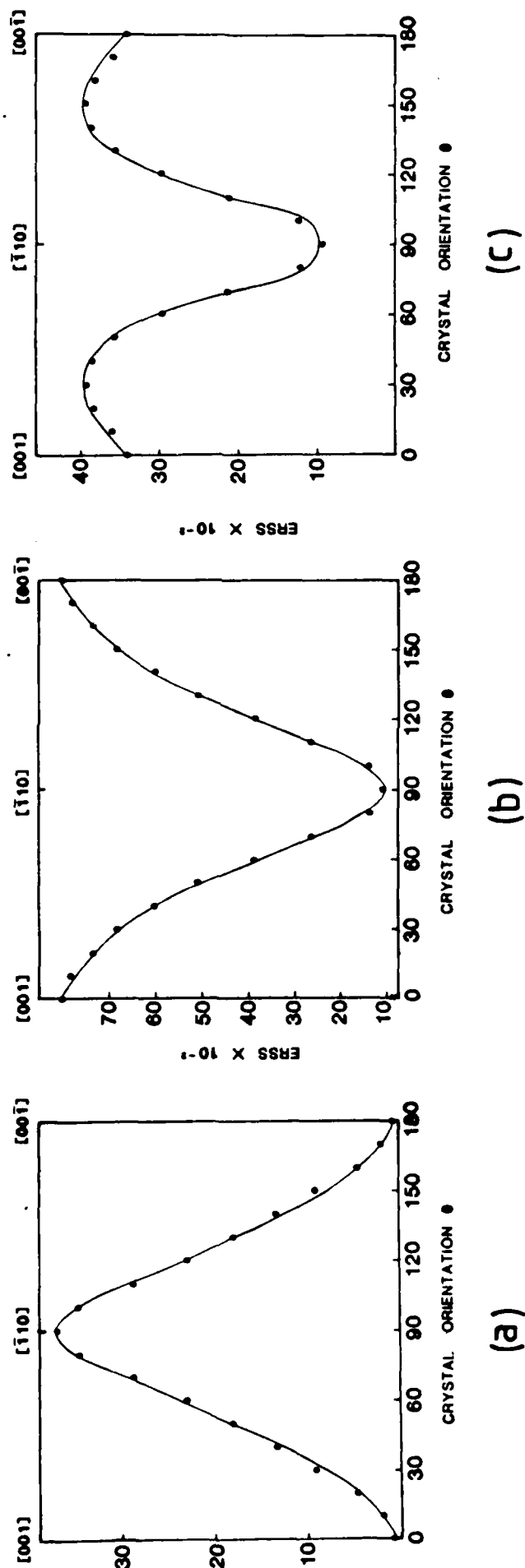


Figure 5 A plot of the effective resolved shear stress (ERSS) against crystal orientation ( $\theta$ ) on the  $\{110\}$  face for the slip systems (a)  $\{110\} [001]$  (b)  $\{110\} \langle 110 \rangle$  and (c)  $\{110\} \langle 111 \rangle$ .

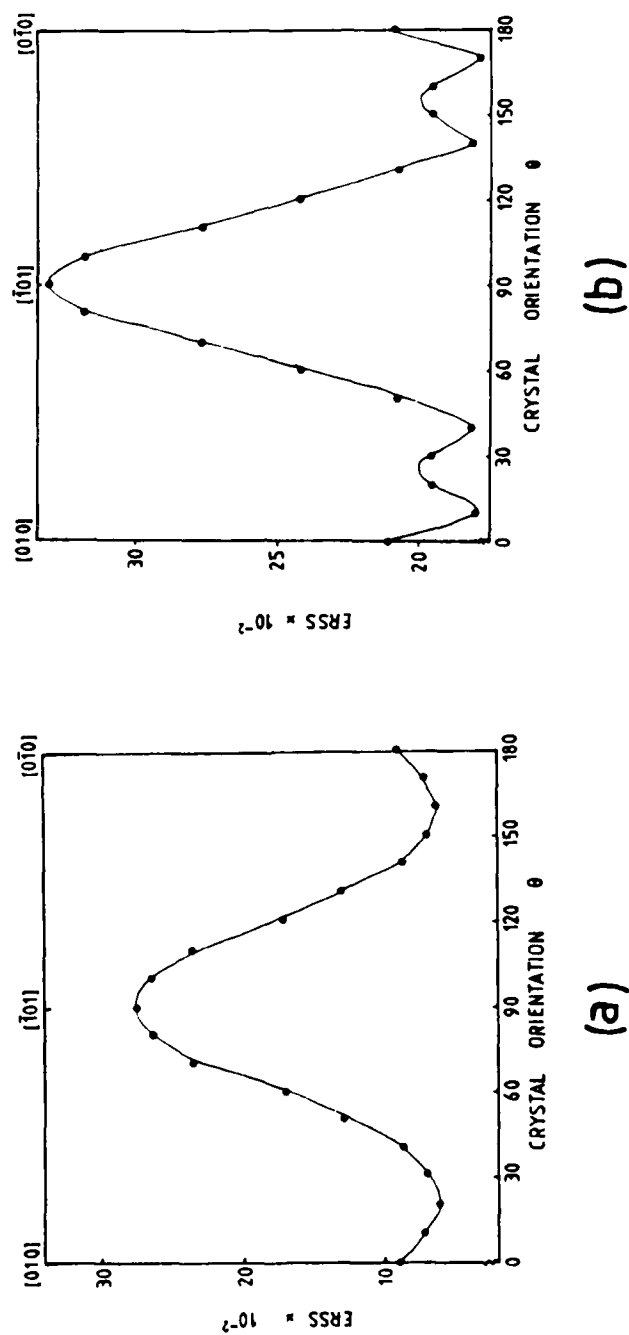
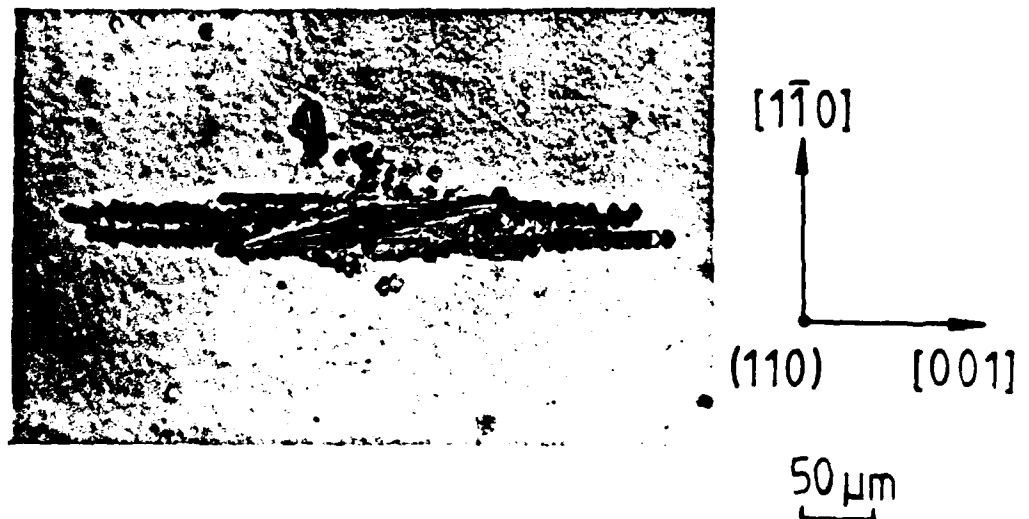


Figure 6 A plot of the effective resolved shear stress (ERSS) against crystal orientation ( $\theta$ ) on the (101) face for the slip systems (a)  $\{110\} \langle \bar{1}10 \rangle$  and (b)  $\{110\} \langle \bar{1}11 \rangle$ .



**Figure 7** An etched indentation mark (load 25g) on the  $(110)$  face of PETN showing the alignment of etch-pits along the  $[001]$  direction.



**Figure 8** The geometry of the etch-pits observed around the indentation marks on the  $(110)$  face of PETN.  
(Scale mark  $10\mu\text{m}$ )

AN X-RAY TOPOGRAPHIC STUDY OF MECHANICALLY  
INDUCED DISLOCATIONS IN PETN

- 1 Introduction
- 2 Experimental
  - 2.1 Crystal preparation
  - 2.2 Deformation methods
    - 2.2.1 Microhardness Indentation
    - 2.2.2 In-situ Tensile Testing
  - 2.3 X-ray topography
- 3 Results
  - 3.1 Topographic assessment
  - 3.2 Characterisation of  
the dislocation loops
  - 3.3 Tensile deformation
- 4 Conclusions



## 1 Introduction

In their classic work, Gilman and Johnston [1] used an etching method to demonstrate that mechanical dislocations can be introduced into a crystal in a controlled manner by impacting the surface with various types of hard indenter. They showed that, in general, the dislocations created in this way have the shape of dislocation half-loops with their ends emergent on the impacted crystal surface.

Similar results have also been achieved for the organic energetic solid PETN [2]. Indentation of the two naturally occurring faces followed by etching, yielded rows of dislocation etch pits extending from the indentation marks in well-defined crystallographic directions corresponding to the intersection of the  $\{110\}$  slip planes with the surface. Unfortunately, however, dislocation etching reveals only the surface intersection of the dislocation loops. It provides no information about the configuration of the dislocations in the bulk of the crystal.

In this section, the technique of X-ray diffraction topography was used to assess the distribution of strain and the nature of the dislocations induced in the bulk of the crystal following local deformation of the surface. The dislocations were characterised using the extinction contrast criteria [3].

## 2 Experimental

### 2.1 Crystal preparation

A crystal of PETN was grown from a seed by the controlled temperature lowering of a saturated ethyl acetate solution, using the conditions specified previously by Halfpenny et al [4]. The crystal exhibited a prismatic habit with dominant  $\{110\}$  and  $\{101\}$  forms. The PETN (initial purity 99.75%) was purified before use by multiple recrystallisation from acetone. The solvents were also distilled prior to use in both recrystallisation and crystal growth.

## 2.2 Deformation methods

### 2.2.1 Microhardness Indentation

Two sections parallel to the (110) plane were cut from the crystal. The first section was deformed by indentation using a Leitz Miniload hardness tester fitted with a standard pyramidal indenter. A single Knoop impression (25g load) and four Vickers indentations (25g load) were made on the cut and polished (110) face. Gross deformation of the second slice was accomplished by squeezing the sample manually on a lateral (101) face, using a pair of pointed tweezers to simulate indentation. Following indentation, the slice was polished to a thickness suitable for topography and washed to remove any damage which may have been introduced by handling.

### 2.2.2 'In-situ' Tensile Testing

Cut and polished samples ( $13 \times 6 \times 1\text{mm}^3$ ) of PETN of slice plane (100) and tensile axis  $(011)_n$  were glued to the platens of a micro tensile stage. This orientation was chosen to yield a high resolved shear stress on the potential slip systems  $\{110\} \langle \bar{1}11 \rangle$  and to allow access to a single strong X-ray reflection for X-ray topography.

Two experiments were carried out. Firstly, a sample was deformed to fracture in order to assess if plastic deformation occurred. Secondly, a more controlled experiment was carried out in which the strain was applied in increments and the sample topographed at each stage until slip was initiated.

## 2.3 X-ray topography

All the topographs were recorded on Agfa Structurix D4 film. The Lang topographs were taken using Copper radiation ( $\lambda_{K_{21}} = 1.54\text{\AA}$ ).  $0.7\text{\AA}$  was selected as the wavelength for topographs taken at the synchrotron source.

### 3 Results

#### 3.1 Indentation Deformation

Figure 1 shows a series of transmission X-ray diffraction topographs of the indented crystal slice. The hardness impressions form a characteristic image in the topographs. The main features of these images are illustrated schematically in the accompanying sketches.

All of the indentation images exhibit a broad line of intensely dark contrast (length  $350\text{ }\mu\text{m}$ ) which bisects the images parallel to the  $[001]$  direction. Comparison with the etched indentation mark, shown in Figure 2, indicates that the alignment and dimensions ( $350\text{--}450\text{ }\mu\text{m}$ ) of these features corresponds exactly to those of the dislocation slip line traces observed by etching. Therefore, the enhanced contrast can be attributed to dislocations, induced by indentation, which glide on  $(1\bar{1}0)$  planes. The resolution of individual dislocations is not expected because of the high density of dislocations around the indentation indicated by etching and the relatively low resolution ( $1\text{ }\mu\text{m}$ ) of the X-ray topographic technique. The outline of the black linear figure defines the boundary of the plastic deformation zone around the indentation. The dislocations contained in this region probably have a loop configuration extending into the crystal and are, therefore, of variable character, having edge, screw and mixed components in the same loop. Consideration of the potential Burgers vectors for dislocation glide on  $(1\bar{1}0)$  and the likely accessibility of suitable strong X-ray reflections indicated that the dislocation loops cannot be characterised on the basis of extinction criteria for this particular experimental geometry. This is confirmed by their visibility in all of the X-ray reflections.

The indentation images also show prominent lobes of dark contrast. The orientation of the lobes varies from reflection to reflection, but always aligns parallel to the diffraction vector. This lobed contrast arises from the elastic strain which is produced around the indentations. From an assessment of the extent of the lobes in the various X-ray reflections, it can be concluded that the elastic strain extends, almost radially, beyond the plastic region for some distance into the lattice.

A small, white, out of contrast zone, noticable at the centre of the images, is due to the total loss of diffracted intensity from a severely distorted region immediately surrounding the indentation mark itself.

A number of different X-ray reflections of the second, grossly deformed, crystal slice are shown in Figure 3. Numerous growth dislocations (G.D.) are observed around the edges of the slice. The majority of these emanate from the two large bands of solvent inclusion (I) and propagate linearly towards the growth faces in both the  $(1\bar{1}0)$  and  $(101)$  growth sectors. A lesser number of straight dislocations also emerge into the  $(110)$  sector from the interior of the crystal. The angle of inclination and the line directions of these dislocations suggest that they originate from the vicinity of the seed. The bands of included solvent probably result from a sudden fluctuation in the temperature during growth. Up to the occurrence of this growth accident, the crystal was relatively free from defects.

In addition to these growth defects, the topographs show considerable darkening around the site of the indentation. The enhanced contrast in this region is due to a dense entanglement of stress induced dislocation loops. Close to the  $(101)$  surface, the dislocations are not completely resolvable, but around the periphery of this strained volume, segments of individual dislocation loops are clearly visible. The geometrical configuration of the loops and their projection on sample orientation confirms that they were nucleated at the  $(101)$  surface before expanding deeper into the bulk on the  $(110)$  slip plane as previously defined from the etching studies.

### 3.2 Characterisation of the dislocation loops

The Burgers vectors of the dislocation loops were characterised using the invisibility criteria  $\mathbf{g} \cdot \mathbf{b} = 0$ , where  $\mathbf{g}$  = the diffraction vector and  $\mathbf{b}$  = the Burgers vector. From the size and geometry of the dislocation loops, it can be concluded that they lie on the  $\{110\}$  plane. This restricts the potential Burgers vector of the specific glide dislocations to  $[001]$ ,  $\langle \bar{1}10 \rangle$  and  $\langle \bar{1}11 \rangle$  ( $|\mathbf{b}| = 0.67\text{nm}$ ,  $1.32\text{nm}$  and  $1.48\text{nm}$ , respectively). The dislocations loops are visible in all but one of the X-ray reflections shown in Figure 3. Visibility in the reflections  $\mathbf{g} = 2\bar{2}0$  and  $\mathbf{g} = 002$  rules out  $\mathbf{b} [001]$  and  $\mathbf{b} \langle \bar{1}10 \rangle$ , respectively, as possible Burgers vectors. Extinction only occurs in the reflection  $\mathbf{g} = 21\bar{1}$ . Therefore, the Burgers vectors of the dislocation loops are characterised as  $[\bar{1}11]$ . The invisibility criteria for the various combinations of Burgers vector and X-ray reflection are summarised in Table 1. Presumably the other equivalent  $\langle 111 \rangle$  type Burgers vectors can also occur. Therefore, the slip system for PETN is defined as  $\{110\} \langle \bar{1}11 \rangle$ .

### 3.3 Tensile Deformation

The tensile sample, prepared and mounted as described above, was put under tension. The strain was increased in increments. In an initial experiment the sample was stressed to fracture in order to compare its behaviour to RDX. Fracture occurred at 50N. Figure 4 shows the results of this experiment.

Figure 4c is an optical micrograph of the surface showing evidence of considerable slip. The orientation and alignment of slip bands correspond to the intersection of the  $\{110\}$  slip planes with the surface. X-ray topographic examination of the sample yielded the evidence shown in Figures 4a and 4b which represent, respectively, the defect structure in the initial and deformed sample. The sample has deformed considerably before fracture to yield dense, but well-defined slip bands. Geometrical calculations prove these to lie in  $\{110\}$  planes.

With the fracture strain defined, a second experiment was carried out in which the stress was applied incrementally and examined by X-ray topography at each stage. Figure 5 shows the consequences of this experiment.

The sample  $13 \times 6 \times 0.7\text{mm}^3$  was cut, washed and polished prior to mounting on the tensile stage. Comparison of topographs before and after mounting showed that no additional defects were generated during the mounting process. Figure 5a shows a topograph of the crystal after mounting. Due to the unusual orientation of the crystal, a complex pattern of growth sectors is imaged. These are identified in the schematic diagram shown in Figure 5b. Additionally, numbers of straight growth dislocations can be seen clearly in the  $\{110\}$  growth sectors.

The crystal was then tensioned under a stress of 40N and the resulting deformation examined by topography. An initial examination with the crystal under tension, yielded a diffuse image due to the interaction of the diffracted X-rays with residual elastic strain in the stressed sample. Release of the stress before X-ray examination produced a more satisfactory result (Figure 5c).

Rows of individual dislocation slip bands have developed parallel to  $[001]$  and which lie in  $\{110\}$  planes. Several of these have been pinned at impurity inclusions (Figure 4c, A and B) which may also be the initiation points of the deformation. The growth dislocations apparently play no part in the generation of the slip bands. It is noteworthy also that the growth dislocations do not move under the applied stress. This is not surprising, since previous topographic examination of growth dislocations in this material have indicated that the growth dislocations were heavily decorated with solvent/impurities which would hinder motion and render the dislocations sessile. [5]

With the experimental geometry used, it was not possible to characterise the dislocations using X-ray topographic methods. This was due principally to the lack of a suitable range of X-ray reflections for this orientation of the crystal. Additionally, the image resolution was rather poor due to the excessive crystal to film distance demanded by the size of the tensile stage.

A solution to this problem could be the use of synchrotron radiation with its improved properties as described in the section on RDX. Regrettably, however, PETN suffered in a similar way to RDX from radiation damage. Significant changes in radiation induced substructure were observed in periods of less than 1 hour (Figure 7).

#### 4 Conclusions

The distribution of strain and the nature and configuration of the dislocations induced by local deformation of the surface of PETN crystals were assessed by transmission X-ray diffraction topography. Several important points are noted below

- 1 Three main regions of strain were identified from the contrast of the images of indentation marks. A highly anisotropic zone of plastic deformation was observed to extend a considerable distance from the point of indentation, reflecting the high plasticity of this solid. The alignment and dimensions of this strained region is consistent with the [001] slip line traces defined by etching. Individual dislocations could not be resolved and the lack of suitable X-ray reflections prevented characterisation of these dislocations. A more symmetrical zone of elastic strain, having an almost radial distribution around the indentation mark, was also revealed. At the centre of the indentation mark, a small region of extreme lattice distortion could also be discerned.

- 2 Loading of the surface with a pointed indenter produced local stresses high enough for the nucleation and subsequent expansion of a series of dense interpenetrating dislocation loops. From the configuration of the dislocation loops and their visibility in various X-ray reflections, the slip system for PETN was assigned as  $\{110\} \langle \bar{1}11 \rangle$ . This confirms the speculations made following indentation and etching examinations.
- 3 Attempts to induce dislocations by tensile deformation were successful. Individual dislocations and slip bands were induced into the solid. These were shown to lie in the  $\{110\}$  planes. The complete characterisation of these dislocations by assignment of Burgers vectors was not possible due to the incompatibility between sample orientation and the availability of suitable X-ray reflections.

### References

- 1 J. J. Gilman and W. G. Johnston in "Dislocation and Mechanical Properties of Crystals", Ed. J. C. Fisher, Wiley, p116 (1957).
- 2 P. J. Halfpenny, K. J. Roberts and J. N. Sherwood, J. Mat. Sci. 19, (1984), 1629-1637.
- 3 B. K. Tanner, "X-ray Diffraction Topography", Pergamon (1976).
- 4 P. J. Halfpenny, K. J. Roberts and J. N. Sherwood, J. Cryst. Growth, 67, (1984), 202-212.
- 5 P. J. Halfpenny, K. J. Roberts and J. N. Sherwood, J. Appl. Cryst., 17, (1984), 320-327.

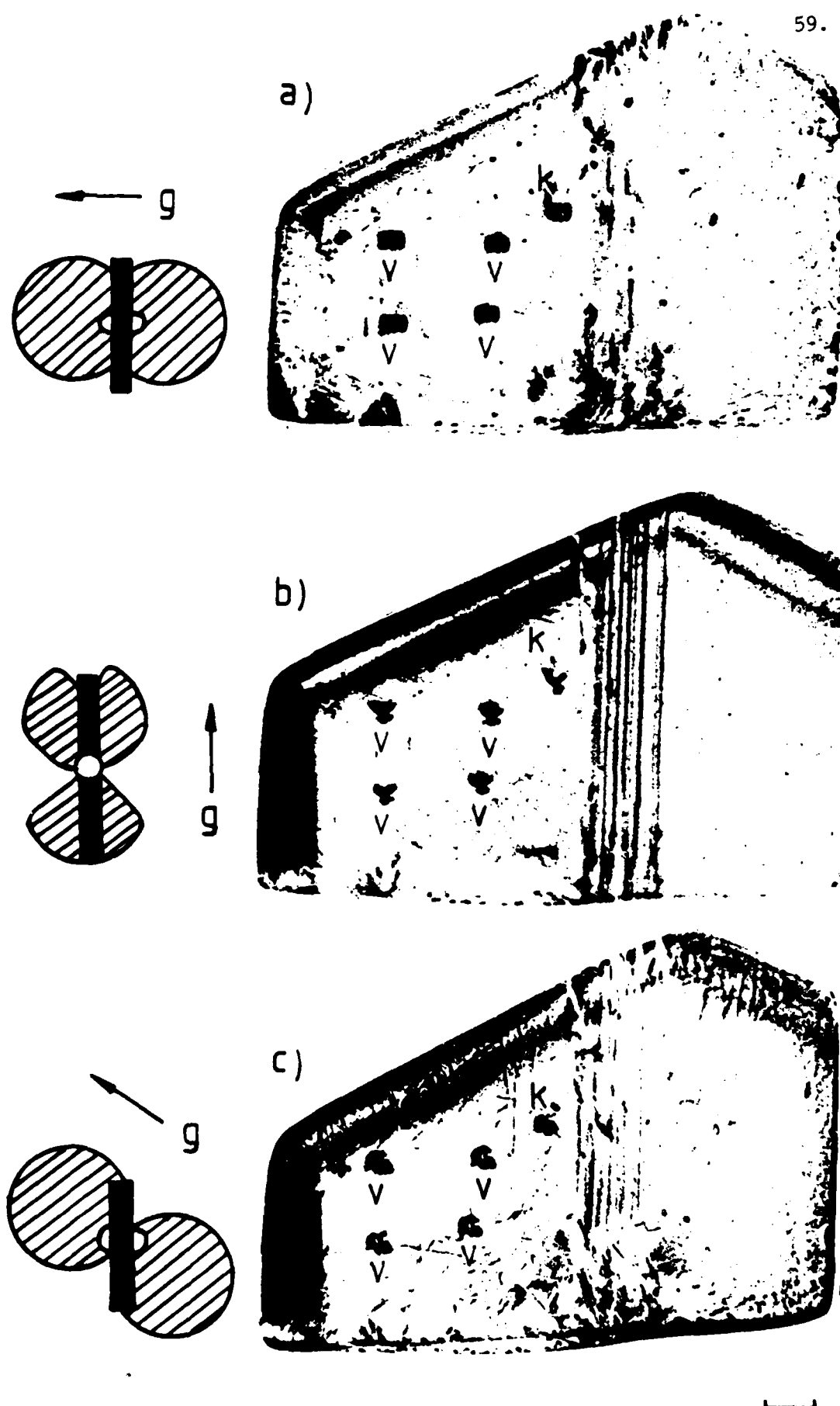


TABLE 1

The contrast criteria for combinations of  
potential Burgers vectors  $\underline{b}$  and  
X-ray  $\underline{g}$  vectors for mechanically induced dislocations  
in PETN.

$\underline{b} \backslash \underline{g}$	$2\bar{2}0$	$002$	$2\bar{2}\bar{2}$	$2\bar{1}\bar{1}$	$21\bar{1}$
$[001]$	0	m	m	w	w
$[1\bar{1}0]$	s	0	s	s	w
$[1\bar{1}1]$	s	m	m	m	0
$[\bar{1}11]$	s	m	s	s	m

s - strong, m - medium, w - weak.



**Figure 1** X-ray topographs of Knoop, K, and Vickers, V, indentation marks on the (110) surface of a PETN crystal  
 a)  $2\bar{2}0$  reflection b)  $002$  reflection c)  $2\bar{2}\bar{2}$  reflection. The small diagrams show the contrast distribution around the indentations in each reflection.

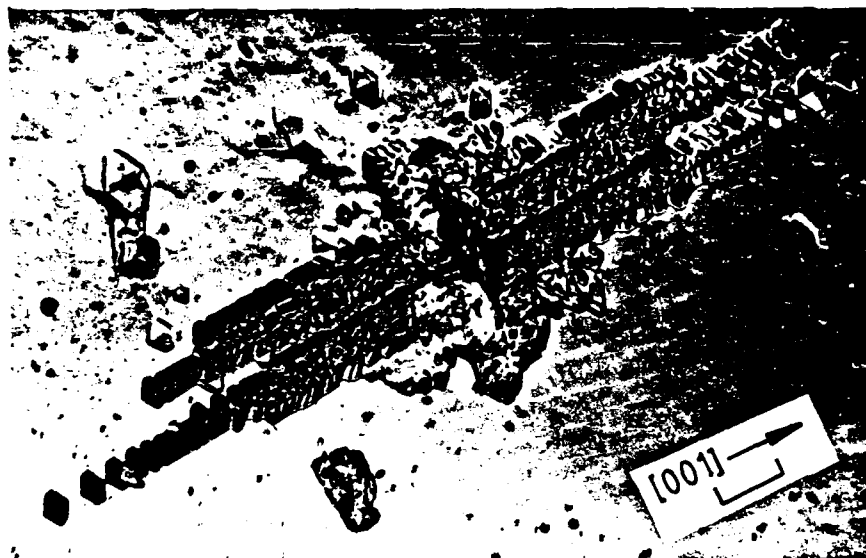


**Figure 2** An etched Vickers indentation mark (25g load) on the (110) face of PETN showing distinct etch-pit alignments parallel to [001]. (Scale mark 30  $\mu\text{m}$ ). (After Halfpenny et al [2]).

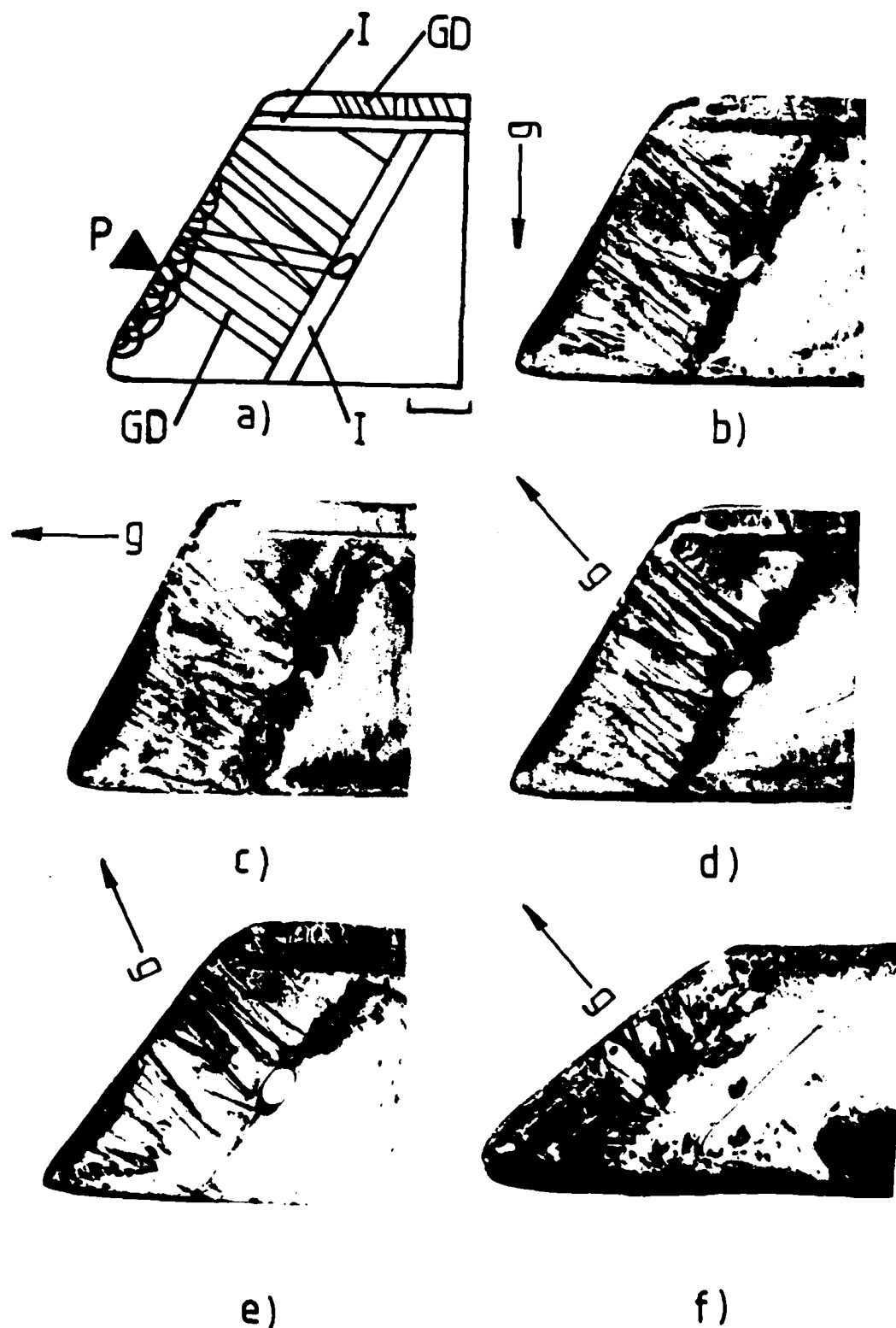
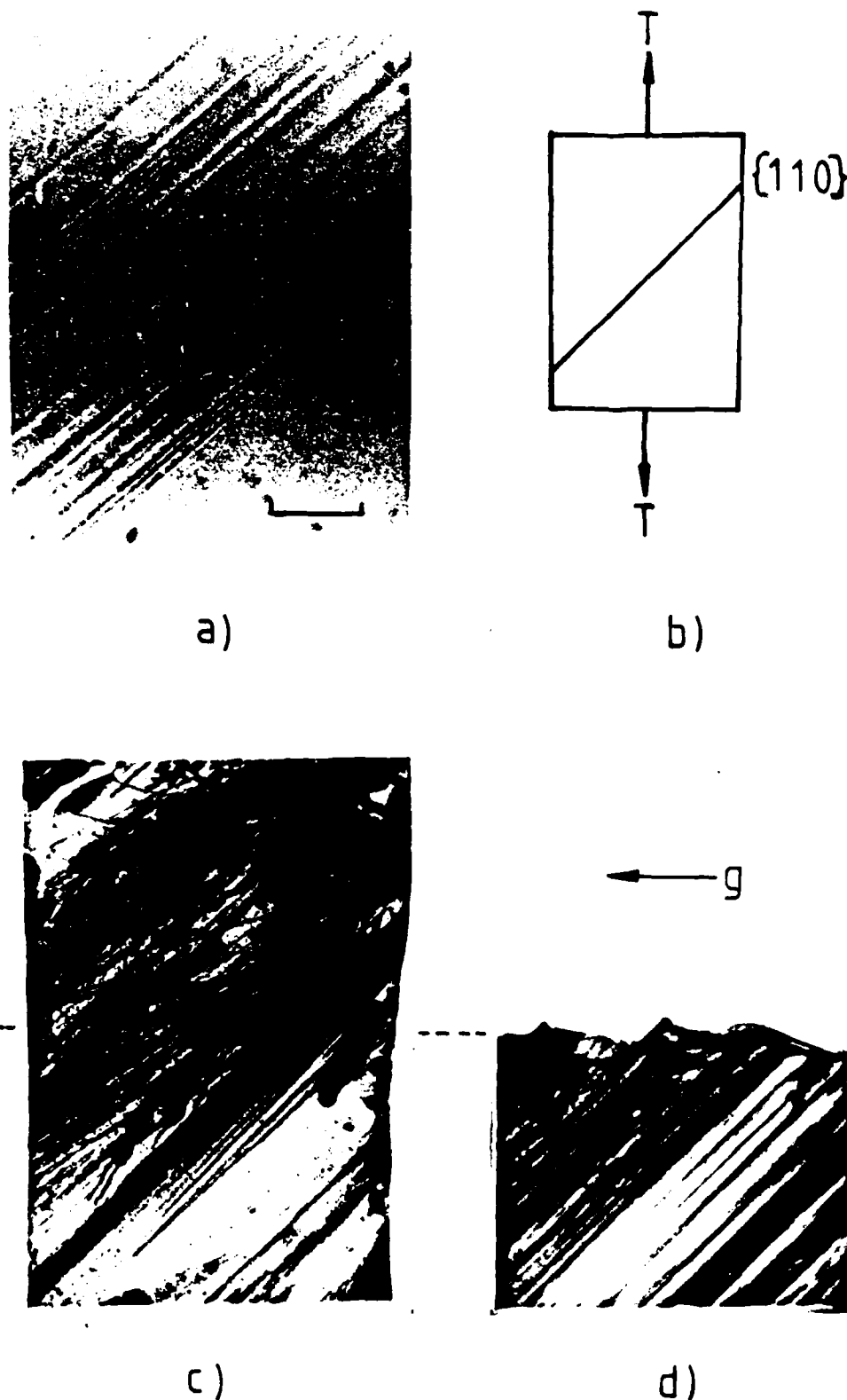


Figure 3 X-ray topographs of the grossly deformed section of PETN  
 a) schematic diagram showing the position of the indentation point, P, growth dislocations, G D, and impurity inclusion bands, I  
 b)  $2\bar{2}0$  reflection c)  $002$  reflection d)  $2\bar{2}\bar{2}$  reflection  
 e)  $211$  reflection and f)  $211$  reflection.

The indentation loops and their strain field can be detected in all topographs except for the  $211$  reflection. (Scale mark 1mm).



**Figure 4** a) Optical micrograph of the surface of a fractured PETN tensile specimen. The slip traces lie at the intersection of the  $\{110\}$  planes with the surface. (Scale mark  $50\mu\text{m}$ )  
 b) Schematic diagram of the tensile specimen.  
 c,d) X-ray topographs (021 reflection) of the tensile specimen c) initial, before deformation d) after fracture (50N,  $6 \times 0.5\text{mm}^2$  cross-section).

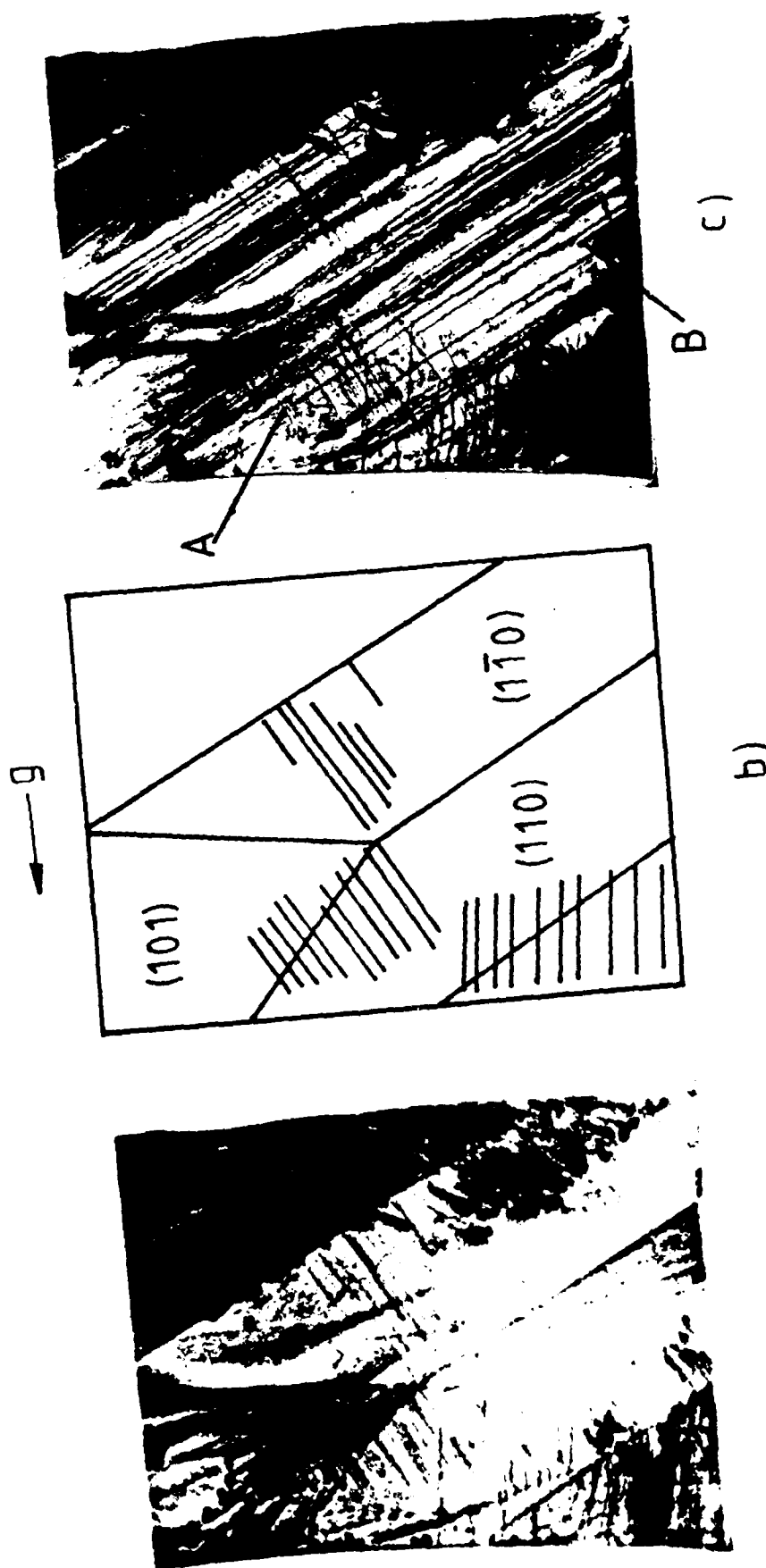
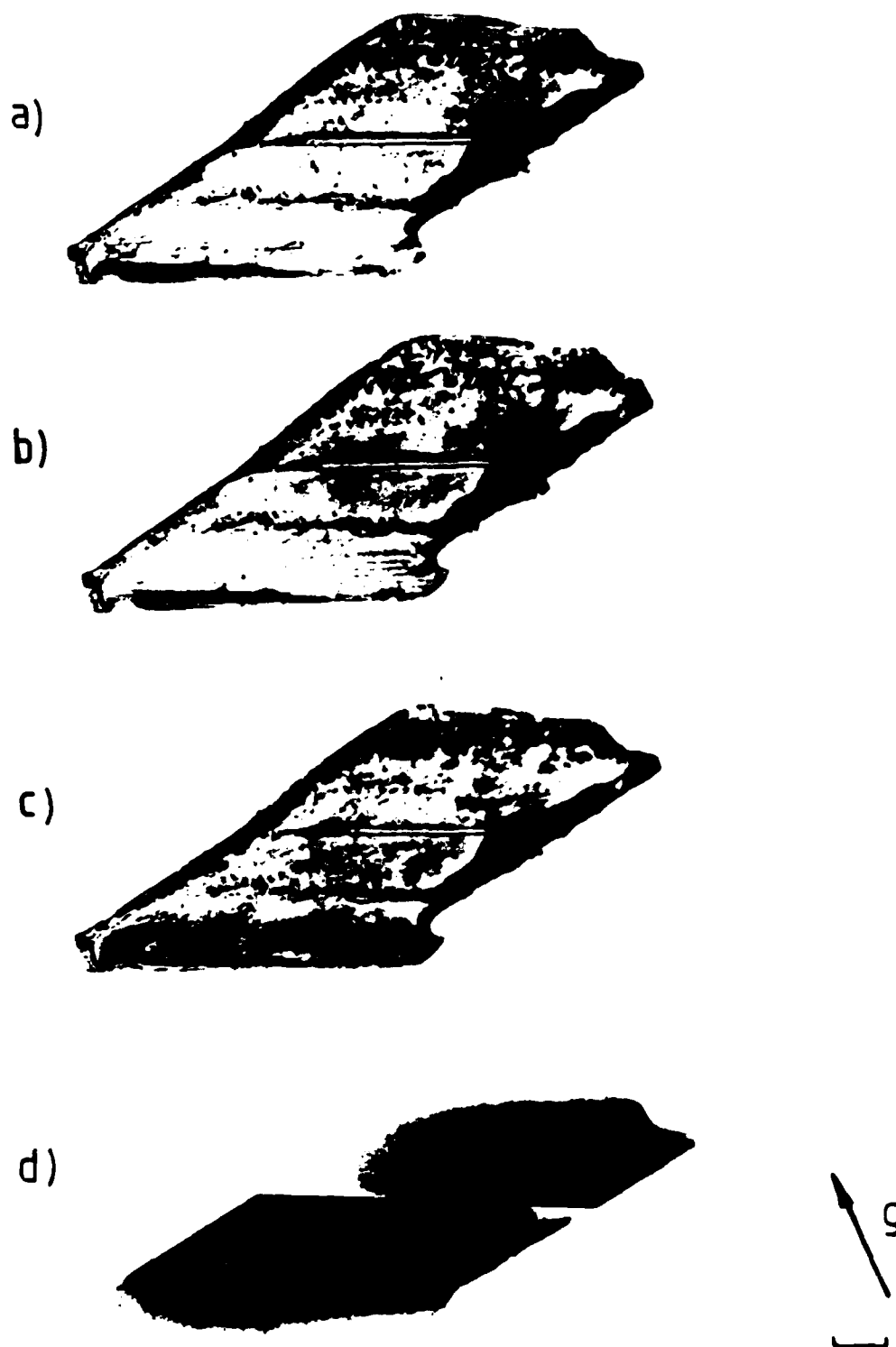


Figure 5 a) X-ray topograph (021 reflection) of a PETN tensile specimen before pulling.  
 b) Schematic diagram identifying the growth sectors and growth dislocations.  
 c) X-ray topograph (021 reflection) of the specimen after tension (40N, 6 x 0.7mm<sup>2</sup> cross-section).



**Figure 6** Synchrotron X-ray topographs (021 reflection) of progressive radiation damage in the synchrotron beam.  
 a) initial b) 1 hour c) 3 hours d) 48 hours after  
 c) showing post-radiation damage. (Goniometer = 0.1 mm  
 $1.0 \text{ \AA}$ ,  $\lambda$  (topograph) =  $0.7 \text{ \AA}$ )  
 (Scale mark 1mm).

END

6-87

Dtic